

SEISMIC IMAGING OF A PORTION OF THE WEST CHABOT FAULT AT
CALIFORNIA STATE UNIVERSITY, EAST BAY

A University Thesis Presented to the Faculty
Of
California State University, East Bay

In Partial Fulfillment
of the Requirements for the Degree
Master of Science in Geology

By
Adrian Thomas McEvelly

December 2018

ABSTRACT

Located along the Pacific-North American plate boundary, the San Francisco Bay Area is home to more than seven million people and no fewer than a dozen active faults. As documented in the United States Geological Survey (USGS) publication: Earthquake Outlook for the San Francisco Bay Region 2014–2043, the Hayward, West Napa, Greenville, Calaveras, and several other faults of the San Andreas Fault system have all produced earthquakes of magnitude 6.0 or greater in the past 150 years, and the occurrence of lower magnitude (<M6.0) earthquakes is not uncommon on these faults as well as the many other faults within the region. The San Francisco Bay region is statistically likely (72%) to produce one or more M6.7 or greater earthquakes before 2043, with the Hayward Fault as the most statistically likely (33%) to produce such an event. Earthquakes are commonly classified by their moment magnitude, a metric that accounts for the area of fault rupture, the average slip distance along the fault, and the force required to initiate the temblor. However, moment magnitude does not consider the qualities of the earth materials through which the rupture occurs, or the depth of the earthquake. While moment magnitude describes the size of the earthquake, strong shaking is a function of the earthquake's source, the path the earthquake travels, and the site conditions.

For site characterization, the direct sampling methods recommended in the California Department of Transportation (Caltrans) Geotechnical Manual are the most accurate method in terms of the range of testable properties, such as shear strength,

porosity, expansive potential, or fluid content. However, direct observation through drilling or excavation, sample recovery, and materials testing procedures may be logistically and economically prohibitive, particularly when assessing seismic risk potential over large urban areas. Moreover, tectonically active regions marked by a series of subparallel, steeply-dipping faults and folds, tend to result in areas of laterally discontinuous geologic units, meaning that the material properties of a single sample of earth material, typically 6.4 cm (2.5") diameter or narrower, may be inappropriate, even for a localized area. Lastly, accessibility issues, due to property ownership, topography, weather, and prohibition of invasive techniques, such as drilling or excavation, may make traditional geologic sampling impossible. However, by actively imparting elastic waves into the subsurface and recording their respective arrival times at known distances from the source along the surface, the seismic wave velocities of the subsurface materials can be determined. Numerous studies including those by Catchings and others at the USGS in recent years have shown that by evaluating the subsurface in terms of seismic velocities and their ratios, informed conclusions may be made regarding the physical qualities of subsurface materials and their propensity for strong shaking and/or liquefaction during a powerful earthquake.

California State University, East Bay (CSUEB), located in Hayward, California, is situated atop the San Leandro Block within the Hayward Fault Zone. The San Leandro Block is an Early Cretaceous to Late Jurassic aged lithotectonic assemblage dominated by ophiolitic serpentized gabbro, intercalated with minor silicic volcanic and marine sedimentary units. The mapped boundaries of the San Leandro Block are defined by the

subparallel, northwest-trending Hayward Fault to the west, and the similarly-trending Chabot Fault to the east; however, geophysical and geological investigations have shown that both the Hayward and Chabot Faults cut through the San Leandro Block in places, and the block is pervasively cut by anastomosing secondary faults. Results from magnetic and gravity surveys across the HFZ described in a 2003 publication by Ponce and others suggest that the SLB dips steeply to the northeast and extends to a depth of at least 7 km. The block itself is approximately 30 km along strike and up to 3 km wide. Locally, units immediately to the east of the San Leandro Block are mapped as Early Cretaceous marine sedimentary rocks of the Great Valley sequence.

The CSUEB campus is located as close as 300 m from the active trace of the Hayward Fault, suggesting that it does not fall within an Alquist-Priolo (AP) zone of required investigation. The AP act, passed in 1972, recommends that California properties whose boundaries lie within the boundaries of an area extending approximately 152 m (500') from the trace of a Holocene-active fault first be characterized for any unidentified Holocene-active faults prior to major construction. The AP act suggests that new construction be set back ~15-m (50') from any Holocene-active faults. The campus does lie within both landslide and liquefaction zones, per the Seismic Hazards Mapping Act of 1990.

In May of 2015, as part of an ongoing collaborative effort led by the USGS to create a 3D velocity model of the San Francisco Bay Area and to characterize strong ground motion recording sites, researchers from California State University, East Bay (CSUEB) and the USGS conducted a seismic survey on the CSUEB campus in Hayward.

The goals of this study were to locate the trace of the West Chabot Fault on the CSUEB campus, determine the character of the underlying bedrock, and measure seismic velocities within the fault zone and near a strong motion recorder located on the CSUEB campus. We deployed a 60-channel, 295-m-long profile of 4.5-Hz horizontal and 40-Hz vertical sensors spaced at 5-m intervals. A 226-kg accelerated weight drop was used to generate P waves for P-wave refraction tomography and Rayleigh waves for V_s evaluation using the multichannel analysis of surface waves (MAS_RW) method. We also used a 3.5-kg sledgehammer and shear-wave block to generate S waves for S-wave tomography and Love waves for V_s evaluation using the multichannel analysis of surface (Love) waves (MAS_LW) method.

I use interpretations of V_p , V_s , V_p/V_s , Poisson's ratio, MAS_RW , and MAS_LW models from this study infer the location of an eastward-dipping, low-velocity zone near the center of the seismic profile that is coincident with the mapped trace of the West Chabot Fault. Higher velocities in the southwest section of the seismic profile are consistent with the mapped and locally-exposed San Leandro Block gabbro. The lower velocities in the northeast section of the seismic profile likely indicate a layer of fill of some thickness, perhaps overlying Great Valley sedimentary units. Finally, the 1500 m/s V_p contour, which is known to correlate with the top of ground water in high-resolution refraction tomography methods, is higher in elevation to the southwest of the low-velocity zone than to the northwest.

SEISMIC IMAGING OF A PORTION OF THE WEST CHABOT FAULT AT
CALIFORNIA STATE UNIVERSITY, EAST BAY

By

Adrian Thomas McEvilly

Approved:

Date:



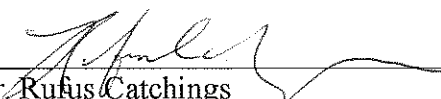
Dr. Luther Strayer

Dec 5, 2018



Dr. Jean Moran

Dec 5, 2018



Dr. Rufus Catchings

December 5, 2018

Table of Contents

Abstract.....	ii
List of Figures.....	ix
List of Tables.....	x
Introduction	1
Background.....	1
Previous Work	3
Purpose of Study	6
Methods	7
Seismic Data Acquisition	10
Seismic Data Processing.....	12
Results.....	13
P-wave refraction tomography	13
S-wave refraction tomography	15
V_P/V_S Ratio.....	17
Poisson's Ratio	18
MAS_RW shear wave velocity model	19
MAS_LW shear wave velocity model	20
Discussion.....	22
Conclusions	26

References.....	27
Figures.....	36
Tables.....	53

List of Figures and Tables

Figure 1. Google Earth image of the East Bay region.....	36
Figure 2. Google Earth image of Chabot Fault and local geology	37
Figure 3. Google Earth image of seismic profile on CSUEB campus	38
Figure 4. Classical Seismic Refraction Method	39
Figure 5. P-wave shot gather showing first arrivals.....	40
Figure 6. P-wave refraction tomography	41
Figure 7. Map of ACWD facilities and monitoring stations near Niles Canyon	42
Figure 8. Fault-related groundwater deflection, Niles Canyon	43
Figure 9. S-wave refraction tomography	44
Figure 10. Changes in V_p , V_s , Density, and Poisson's Ratio due to water saturation	45
Figure 11. V_p , V_s , and V_p/V_s values in both dry and saturated fault zones	46
Figure 12. V_p/V_s ratio model.....	47
Figure 13. Poisson's ratio model.....	48
Figure 14. 2-D MAS_RW shear wave velocity model	49
Figure 15. 2-D MAS_LW shear wave velocity model	50
Figure 16. Geologic model: P-wave data, tomography shown	51
Figure 17. Geologic model: P-wave data	52

List of Tables

Table 1. P- and S-wave acquisition and processing information53

Table 2. GPS coordinates of geophones along seismic profile54

Table 3. ACWD groundwater data from selected sites near Niles, California55

INTRODUCTION

Background

The Chabot Fault system (CF) trends subparallel to and is part of the larger, active Hayward Fault Zone (HFZ) in the San Francisco Bay area, located in the Coast Ranges physiographic region of California (Fig. 1) (Graymer, 2006). The CF strikes $\sim 325^\circ$, parallel to the Hayward Fault (HF), and extends ~ 41 km from just northwest of Niles Junction, where it merges with the Mission Fault (Fig. 2), to just south of the University of California Memorial Stadium in Berkeley, where it merges with the HF (fig. 1). Since at least 1956, the CF has been identified and mapped as a two-strand fault system (Robinson, 1956), consisting of the East (ECF) and the West (WCF) Chabot faults. Modern mapping of the CF shows both strands dip steeply to the east in cross-section (Graymer, 2006; Ponce, 2003). The ECF is mapped as a normal fault, whereas current geological maps for the WCF (Graymer, 2006) do not indicate a sense of direction. The locations of both the ECF and WCF are mapped as approximate or inferred by Graymer (2006).

The CF is traditionally mapped (Graymer, 2000; Case, 1968; Radbruch, 1969; Robinson, 1956) as a discontinuous contact between the San Leandro block (SLB), a lithotectonic unit composed chiefly of gabbro and serpentinite of the Jurassic-aged Coast Range Ophiolite (CRO) intercalated with minor silicic volcanic and marine sedimentary units, and the and the Early Cretaceous marine sedimentary units of the Great Valley sequence (GVS), and is mapped as such a contact through the CSUEB campus (Fig. 3). However, there are several documented locations within and adjacent to the USGS

Hayward 7.5-minute Quadrangle of a conformable contact between the Knoxville Formation of the GVS, an Early Cretaceous and Late Jurassic marine shale, and the Jurassic ophiolitic rocks of the CRO (Graymer, 2000), suggesting the CF cuts through adjacent units in these locations. Documentation of hillslopes that were cut and graded during construction at Montera Middle School in the Montclair District of Oakland in 1959 record a conformable depositional contact between sandstone and shale units of the Great Valley Joaquin Miller Formation and serpentinite of the CRO (Oakeshott, 1982) (fig. 1). However, Case (1968) describes the ECF as the contact between the older Knoxville formation to the southwest and younger Joaquín Miller formation to the northeast. Thus, the CF is currently understood to both bound the CRO and the GVS, but the CF also cuts through individual rock units of both CRO and GVS at other locations along its trace, leaving the CRO-GVS depositional contact intact.

Offset gravel deposits documented along the ECF indicate an age of previous activity no younger than Pleistocene, and the CF is cut by the more recently active Mission Fault (Fig. 2), (Jones and Graymer, 1993). The Chabot Fault system is not known to be Holocene active and is not specified as an Alquist-Priolo earthquake fault (California Geological Survey (CGS), 2018). Although recent activity has not been recorded on the CF, it is part of a system of faults in the Niles area that includes Holocene active faults, including the Mission Fault (Aagard, 2016).

Previous Work

Tectonics

Past studies of the tectonic relationship between the Chabot and Mission faults (Jones and Graymer, 1993) and stratigraphic offsets of Pleistocene-aged gravels found at Lake Chabot and in the Niles area (Graymer, 1995) suggest that the CF is a fault no younger than Pleistocene age that has accommodated at least 23 km of right-lateral offset within the HFZ since its inception. More recent studies on the CF include the joint CSUEB-USGS 2016 East Bay Seismic Investigation (Strayer et al., 2017), which imaged both strands of the CF, and the 2013 CSUEB-USGS Warren Hall Implosion seismic survey conducted on the CSUEB campus (Catchings et al., 2015). Both the ECF and WCF appear on geologic maps of the Hayward Quadrangle, dating back to at least 1956 (Robinson, 1956; Case, 1968; Radbruch, 1969; Graymer, 2000).

Site Characterization

The field of applied geotechnical engineering deals with characterizing and mitigating geological hazards. Three such interests are the location and history of faults and landslide slip planes, local groundwater conditions, and the depth to coherent bedrock, which may be overlain by units of unconsolidated material, such as fill, colluvium, or landslide deposits (CGS, 2018). A variety of methods are employed to characterize site hazards, which can be subdivided into two approaches, invasive and noninvasive (Waltham, 2009).

Invasive techniques, such as drilling and the excavation of trenches and test pits, involve displacing and physically interacting with the earth material destined to be

characterized (Saari, 1988). Data recorded by a field geologist during drilling and sampling may include geologic descriptions from known depths, relative material resistance recorded as drill depth over time and blow counts from drive samples, suspected fracturing or other void spaces due to drill fluid loss, and the presence of any groundwater (Fusee, 2016). Samples may be further tested to determine qualities, such as water content, porosity, shear strength, or density (Caltrans 2018). Furthermore, the borehole may then be used to install monitoring equipment, such as piezometers to monitor groundwater levels or inclinometers to record displacement at depth within the column of the borehole (Waltham, 2009). Thus, drilling and the ability to recover undisturbed samples from boreholes can provide a great deal of information about earth materials in a single dimension, projected from a point on the surface, without a great deal of disturbance to the subsurface. Trench and pit excavations offer the opportunity to visually assess a two-dimensional cross-section of the subsurface and are particularly useful for seismic or landslide investigations where faults and slip planes can be visually identified and relative ages can be determined in the field. Organic materials, fossils and charcoal, for example, may be radiometrically dated to provide absolute dates of units and tectonogenic deposits (McCalpin, 1996). When such surveys are concluded, trenches and pits must be backfilled and engineered according to code before further development (Caltrans, 2018). Thus, excavation techniques are useful for characterizing structural macrofeatures, such as faults and landslides in cross-section, but require permitting, machinery, operators, and access, and the site must be repaired once the survey is completed.

Noninvasive techniques for site characterization include several geophysical methods, each with slightly different, overlapping applications (Reynolds, 2011). Ground penetrating radar is a useful tool that can be operated by a single user and is often used for locating utilities, storage tanks, and buried unexploded ordnances, but with depth-of-penetration limitations that rarely exceed 10 m (Reynolds, 2011; Waltham, 2009). Electrical resistivity surveys can be effective for determining the location of groundwater but do not give information about density or shear strength, and gravity surveys can infer mafic rocks like those for the SLB, but gravity surveys are areal in acquisition and cannot alone provide information about how structures may change with depth (Keller, 1979; Reynolds, 2011). Reflection seismology is an efficient and effective method of evaluating the subsurface structure when the subsurface geologic materials are sub-horizontal. As such reflection seismic methods are often used to evaluate geological contacts, changes in physical properties, faults, and geological anomalies in layered materials (McEvelly, 1979). While these reflectors give useful structural information, reflection surveys do not provide direct velocity values (Reynolds, 2011). Additionally, our study area is one where steeply-dipping and sub-vertical faults and contacts tend to be the norm, making the reflection method largely unusable.

Active-source seismic refraction surveys have been shown to be effective in characterizing areas that have high variability in physical properties, such as landslides (Uhlemann, 2016), or high-angle faults in highly weathered, structurally complex terranes (Catchings et al., 2014). Furthermore, it has been demonstrated that both Poisson's and V_p/V_s ratios are useful indicators of water-saturated faulted rock

(McEvelly, 1974; Castagna, 1985; Gregory, 1976; Catchings et al., 2007, 2014). Finally, seismic refraction methods can be used to locate faults that lack surface expression (Catchings et al., 2014; Rosa et al., 2016). As the subsurface for the CSUEB seismic profile potentially consists of steeply-dipping, weathered, crystalline and massive sedimentary rocks, engineered fill, and a high-angle fault obscured by an asphalt parking lot, an active-source, I determined that a high-resolution seismic refraction survey is an appropriate and effective method for investigating the CSUEB West Chabot fault.

Purpose

This research was conceived from an interest in using geophysical techniques to verify the mapped (approximated) location of the WCF (Graymer, 2000, 2006; Case, 1968; Radbruch, 1969; Robinson, 1956) where it cuts through the CSUEB campus in Hayward, California. As the CF cuts through units of both CRO and GVS and delineates the contact between the two assemblages, my study also sought to locate the fault in reference to these two geologic units and to describe the dip of the WCF. Finally, by mapping the 1500 m/s V_P contour, variations in the depth of water-saturated subsurface materials can be determined (Catchings, 1999a, 1999b; 2001, 2006, 2009, 2013, 2014, 2017).

METHODS

Classical Seismic Refraction: Method and Theory

The seismic refraction method is a minimally-invasive subsurface exploration method, wherein energy in the form of elastic waves is imparted into the subsurface using an active source, such as a sledgehammer, accelerated weight drop, or contained explosion (Redpath, 1973). The elastic waves are converted from mechanical energy to electrical energy by geophone sensors that are placed in the ground and connected to a seismograph, which records both the signal from the geophone sensors as well as the precise time the signals are received (Fig 4).

When P and S waves encounter a vertical velocity contrast in the subsurface, the amount and direction of travel change according to Snell's Law

$$\frac{\sin \theta_i}{\sin \theta_r} = \frac{V_1}{V_2} \text{ (general refraction),} \quad (1)$$

where V_1 is lower than V_2 , V_1 is the velocity of the upper layer, V_2 is the velocity in the lower layer, $\sin \theta_i$ is the angle of incidence, and $\sin \theta_r$ is the angle of refraction (fig. 4) (Dobrin, 1960; Redpath, 1973; Sharma, 1986; Burger et al., 2006; Reynolds, 2011).

When the incident angle is such that $\sin \theta_i$ is equal to $\frac{V_1}{V_2}$, $\sin \theta_r$, θ_r is equal to 90 degrees.

This so-called critically refracted wave travels horizontally along the velocity interface between the two units, at a velocity greater than those waves travelling structurally higher.

Critically refracted waves are described by the equation:

$$\sin \theta_{i_c} = \frac{V_1}{V_2}, \quad (2)$$

where $\sin \theta_{i_c}$ is the angle of critical refraction. When the incident waves approach the boundary of velocity contrast at the critical angle described by equation (2), the critically refracted waves travel along the boundary at velocity V_2 ; furthermore, secondary critically reflected waves are generated in layer V_1 (Dobrin, 1960; Redpath, 1973; Sharma, 1986; Burger et al., 2006; Reynolds, 2011). A portion of the critically refracted waves reach the surface, where they are detected by geophones (Dobrin, 1960; Redpath, 1973; Sharma, 1986; Reynolds, 2011). The travel times of refracted waves recorded at known distances on the surface are described by the equation

$$Time_n = \frac{x}{V_n} + \frac{2}{V_n} \sum_{i=1}^{n-1} h_i \frac{\sqrt{V_n^2 - V_i^2}}{V_i} \quad (3)$$

where $Time_n$ is the travel time of refracted waves of a subsurface having n layers, x is the distance from source to geophone sensor, h_i is the thickness of the i -th layer, and V_n and V_i are the velocities of the n -th and i -th layers (Redpath, 1973; Burger et al., 2006). Furthermore, rearrangement of equation (3) allows us to calculate thickness (h_{n-1}) using the intercept time when $x = 0$, and velocities (V_n) by taking the inverses of n slopes (Redpath, 1973; Burger et al., 2006).

Seismic Refraction Tomography Method

P- and S-wave refraction tomography velocity models were developed using their respective first-arrival travel times with the inversion algorithm of Hole (1992). An initial starting model is required, which was developed from 1-D analysis of several shotgathers along the seismic profile. P- and S-wave velocity models were parameterized into 5 x 5-m horizontal and vertical grid intervals based on geophone and shot spacing, as opposed to an assumed number of layers of increasing velocity. Hole's (1992) nonlinear travel-time tomography method uses a finite-difference algorithm to solve the eikonal equation to compute first-arrival travel times from the source to the receiver, and the model is iteratively updated using backprojection. We ran multiple iterations of both the P- and S-wave velocity models. Determination of the optimal tomographic model requires basic informed assumptions about the material and structure within the survey area. Initial iterations show laterally homogenous strata, which was not a reasonable result from my knowledge of our study area, where at least two distinct units at or near the surface are separated by a mapped fault. Furthermore, steeply-dipping subparallel faults, which represent the overall dextral strike-slip tectonic style of the region, generally do not result in lateral geologic continuity, particularly along sections that are tangential to the strikes and axes of faults and folds, respectively. Thus, I chose iteration 25 as the optimum P-wave velocity model, and iteration 18 as the optimum S-wave velocity model

The MASW Method

The Multichannel Analysis of Surface Waves (MASW) method uses the dispersive property of surface waves (Rayleigh and Love waves) to investigate shear-wave velocities in the shallow subsurface and is often used in geotechnical site studies (Park et al., 1999; Xia et al., 2000; Pujol, 2003; Ivanov et al., 2003, 2013; Miller et al., 1999; Park, 2013; Odum et al., 2013). In the analysis of the CSUEB data, dispersion curves were constructed using the common mid-point cross-correlation method (Hayashi, 2003; Hayashi and Suzuki, 2004); the fundamental mode dispersion curves were manually picked and iteratively inverted using a non-linear, least-squares method (Hayashi et al., 2016; Geometrics, Inc., 2016). The starting model parameters assumed 40 m depth and 10 layers with increasing thickness with depth. The MASW methods combine multiple, serial, 1-D inversion results to construct continuous 2-D shear-wave velocity models along the seismic profile.

Seismic Data Acquisition

In May 2015, CSUEB and the USGS acquired high-resolution P- and S-wave seismic data along a two-dimensional (2D) profile across the mapped trace of the WCF, located beneath a parking lot on the Hayward campus of CSUEB (fig. 3). The seismic profile was 295 m long and trended southwest to northeast. Small holes were drilled in the asphalt to provide secure coupling between the geophones and the parking lot ground surface. Sixty vertical-component (40-Hz) and horizontal-component (4.5-Hz) geophones were deployed at 5 m spacing to record P- and S-wave seismic data. To

generate P-waves, a 226-kg accelerated weight drop (AWD) was used to strike a steel plate placed on the ground surface; the weight was driven normal to the plate. S-waves were generated by striking an aluminum shear wave block with a 3.5-kg sledgehammer, parallel to the ground surface and perpendicular to the strike of the seismic line. A total of six sledgehammer shots were recorded at each geophone, three on each end side of the shear-wave block. One shot per geophone was used for P-wave acquisition, apart from the end shots, where 10 AWD shots were stacked to increase the signal-to-noise ratio. We used the ‘shoot-through’ method, whereby every geophone location is also a shot location, ensuring the densest possible raypaths. P- and S-wave sources were co-located with each of the 60 vertical- and horizontal component geophones installed along the 295-m seismic line. Station 1 was located at distance meter 0 located at the southwest end of the seismic line, and station 60 was located at distance meter 295 at the NE end of the seismic line. Seismic data were recorded on a 60-channel, Geometrics StrataVisor RX-60™ digital seismograph, with a 24-bit analog-to-digital converter; the seismograph was connected to the P- and S-wave geophone sensors using standard refraction cables. Acquisition parameters are described in Table 1. Geophone locations (Table 2) were recorded using the Promark 300, real-time kinematic (RTK) GPS system, with theoretical accuracies of approximately 2 cm. Elevation along the seismic line varied by approximately 4 m.

Seismic Data Processing

In preprocessing, the seismic data were first downloaded from the two Geometrics StratavisorTM seismographs via removable magnetic tape to a workstation, where the P- and S-wave data files were assembled into two individual P-wave and S-wave data sets. I visually inspected each shot gather for trace signal quality and shot propagation. A usable shot gather displays clearly identifiable first arrival of the energy from each shot (Fig. 5). The depth of resolution for P- and S-wave surveys depends on identifying shots that are able to travel long raypaths and may therefore increase with the length of the survey line and the energy from the source. Traces where the first arrivals cannot be determined were replaced with a zero trace. Cultural and background noise, insufficient signal propagation, poor sensor-to-ground coupling, faulty geophones and cables, and operator error during any stage of acquisition are all factors that can contribute to poor data quality. Individual shot traces were then grouped by shot location into shot gathers. Multiple shot traces sharing a common shot point (for example, P-wave end shots) were additively stacked into a single trace to improve the overall signal-to-noise ratio, and opposite polarities of S-wave data were corrected before they are stacked into a single trace. The survey geometry was then added to each shot record to include source and receiver locations, offset, and elevations. Timing of each shot record was examined to correct for either early or delayed start times. A bandpass filter was applied to the P-wave dataset, and notch and bandpass filters were applied to the S-wave dataset before picking first arrivals (Table 1).

RESULTS

For the purpose of describing and referring to contour lines and overall shapes indicated on the seismic models, the following terms are hereby defined: *concave-up* refers to a parabolic shape, where the contour lines slope upward and away from the vertex of the curve, roughly resembling the trough of a wave. *Concave-down* refers to a parabolic shape, where the contour lines slope downward and away from the vertex of the curve, roughly resembling the crest of a wave. The so-called *axes* of these shapes correspond to the axis of symmetry that passes through the vertex of a parabola. It is important for the reader to keep in mind that the data plotted in the following models are seismic velocities and their ratios and do not necessarily directly represent the structure of the surveyed area.

P-wave Refraction Tomography (V_P) Model

P-wave velocities (V_P) range from approximately 600 m/s at the surface to more than 3200 m/s at depths of about 50 meters below the ground surface (fig. 6). The maximum imaged depth of the P-wave tomography model is approximately 60 m, about 1/5 of the length of the seismic line. V_P tomography reveals three distinct lateral velocity gradients, roughly defined by meters 0-100 (southwest), 100-200 (center), and meters 200-295 (northeast) of the seismic profile.

V_P values observed in the southwest (0-100 m) section of the seismic profile range from 1500-3200 m/s. The velocity contour lines develop into a concave-down feature starting at approximately 2000 m/s at 5 m depth. This feature increasingly steepens with

depth to the bottom of the profile. The velocity gradient of the southwest section is the most laterally continuous. Average gradients increase at approximately 66 m/s per meter of depth in the upper 15 m and drop to approximately 17 m/s per meter of depth thereafter. The higher rate of increase in the top 15 m may be due to the increasing compaction of fill material due to lithostatic pressure. Additionally, the outer few meters of the SLB should be expected to have undergone some degree of weathering; outcrops of the SLB on the CSUEB campus are composed of weak, highly fractured, weathered gabbro that breaks and crumbles easily. Thus, a gradational, rather than an abrupt change in velocity between geologic units is expected. The lower rate of change in velocity, specifically seen at depths greater than 15 m along distance meters 0-100, are beyond the outer weathering zone of the gabbro; thus, velocities likely increase as rock quality and overburden increase, but velocities are expected to increase at slower rate through the more intact, crystalline rock.

V_P values observed in the center (100-200 m) section of the seismic profile range from approximately 1200 m/s to a maximum of approximately 3000 m/s. V_P contours are subhorizontal in the upper 15 m, up to approximately 2200 m/s. At 15 m and below, V_P contours become convex between distance 100-150 m; velocity contours 2500 m/s and greater dip steeply to the northeast. Between distance 170-200 m and below depths of 20 m, the velocity contours steepen noticeably. Centered at distance meter 165 along the profile at 20 m depth is a closed 2500 m/s V_P contour. The velocity gradient of the top 15 m in the center section of the seismic line is approximately 60 m/s per meter of

depth. Below depths of 20 m in the center section, there is little lateral continuity of observed velocities.

V_P values observed in the northeast (200-295 m) section of the seismic profile range from approximately 600-2000 m/s. Velocity contours show an overall convex shape to a depth of approximately 35 m, where V_P is roughly equal to 1700 m/s. The lowest point of this convex trend dips steeply to the southwest. Below 35 m depth, velocity contours trend to near vertical. The average velocity gradient for the northeast section is approximately 24 m/s, per meter of depth.

In general, observed V_P is highest to the southwest and decreases to the northeast. Velocity contours in the southwest trend concave-down, and concave-up in the northeast. However, there is a high-velocity (2500 m/s) anomaly between distance 150 and 180 m, centered at approximately 20 m depth. The V_P gradient ranges approximately 17-66 m/s per meter of depth.

S-wave Refraction Tomography (V_S) Model

S-wave velocities (V_S) range from approximately 330 m/s at the surface to more than 800 m/s at depths of about 30 m below the ground surface (fig. 9). The maximum imaged depth of the S-wave tomography model is approximately 40 m, approximately 1/7 the length of the seismic line, more shallow than that in the V_P model. This is likely due to the more energetic source used for the acquisition of V_P data. The V_S tomography image reveals three distinct velocity gradients, roughly defined by meters 0-100 (southwest), 100-200 (center), and meters 200-295 (northeast) along the seismic profile.

V_S values observed in the southwest (0-100 m) section of the seismic profile range from approximately 510-810 m/s. The velocity contours dip down to the northeast starting at approximately 650 m/s at 5 m depth and they increasingly steepen with depth to the bottom of the profile. The velocity gradient of the southwest section is the most laterally continuous; average values are approximately 10 m/s per meter of depth in the upper 15 m and decrease to approximately 6 m/s per meter of depth thereafter.

V_S values observed in the center (100-200 m) section of the seismic profile range from approximately 480-700 m/s. V_S velocity contours are sub-horizontal in the upper 20 m, up to approximately 600 m/s. At 20 m and below, V_S velocity contours develop into a concave-up feature to a depth of about 32 m; the dip of the feature steepens thereafter. The velocity gradient of the top 20 m in the center section of the seismic line is approximately 5.5 m/s per meter of depth, and decreases to approximately 3.5 m/s per meter of depth below 20 m.

V_S values observed in the northeast (200-295 m) section of the seismic profile range from approximately 330-670 m/s. Velocity contours are concave-up to 20 m depth, where V_S is roughly 450 m/s. The axis of this concave-up feature dips near vertical. Below 20 m, velocity contours trend subparallel and dip to the northeast. The average V_S gradient for the northeast section is approximately 5 m/s per meter of depth.

In general, observed V_S are highest to the southwest and decrease to the northeast. Velocity contours in the southwest form a gently-sloping concave-down trend that dips to the northeast. The V_S gradient ranges from 3.5-10 m/s per meter of depth.

V_P/V_S Ratio Model

The ratio of V_P/V_S values may be used to identify groundwater-saturated, pulverized rock material that can indicate a fault trace. As the percent water saturation in a rock increases, V_S decreases consistently. V_S is also known to decrease within materials that possess low shear strength, such as fractured rock within a fault trace. V_P also decreases gradually with increasing water content up to about 90% saturation, at which point V_P increases sharply (Fig. 10). Thus, the ratios of V_P/V_S may be used to identify areas within the model likely to be composed of crushed and faulted saturated material (Fig. 11) (Catchings 2014).

V_P/V_S ratios range from approximately 1.7-4.4 (fig. 12), with the majority of the lower (<3.5) ratios occurring between distances 0-30 m and 190-295 m of the seismic profile. Between distance meters 30 and 190 at depths of 15 m and below, V_P/V_S ratios are 3.5 or greater. Centered at distance 160 m along the seismic profile at a depth of 20 m, we see a discrete zone of high (>4) V_P/V_S ratios in the model, bound by significantly lower V_P/V_S ratios with increasing depth and to the northeast. A second zone of anomalously high V_P/V_S ratios occurs 40 m to the southwest of the first zone, separated by a near-vertical zone of lower (-0.1) V_P/V_S ; this second feature shows increasing V_P/V_S ratios with depth. The maximum depth of the V_P/V_S model is constrained by shallowly penetrating S-waves to a maximum depth of approximately 40 m below the surface.

Poisson's Ratio Model

Poisson's Ratio (ν) is an elastic parameter that describes the degree to which a material expands in directions perpendicular to compression. For example, a stopper made of rubber, which has a Poisson's Ratio of 0.5, may be difficult to slide into the neck of a bottle due to the tendency of the rubber to expand when compressed. A stopper made of cork, with a Poisson's Ratio of 0.0, does not expand laterally when compressed and is easier to slide into place. Poisson's Ratio is unitless and can be expressed in terms of a material's seismic velocities as follows:

$$\nu = \frac{[(V_P/V_S)^2 - 2]}{[2(V_P/V_S)^2 - 2]} \quad (4)$$

The values for Poisson's Ratio vary between about 0.2 and 0.5 for most crustal material; Poisson's Ratios of about 0.44 and higher tend to correlate with the top of groundwater (Fig. 10) (Catchings 2014).

Values for ν range from approximately 0.30 to 0.47 in the Poisson's ratio model (fig. 13). Lower (<0.44) values are concentrated in the upper 7 m of the subsurface, primarily between distance meters 200 and 295 of the seismic profile. Between approximately distance meters 10 and 200 of the profile and below depths of about 7 m, Poisson's ratio values range from 0.44-0.47. Between distance meters 25 and 180 along the seismic line, the $\nu=0.44$ contour is approximately 5 m below the surface, and dips abruptly to vertical near distance meter 200. As a whole, Poisson's ratios in this area

increase with depth, with the exception of a zone located between distance meters 150-200 on the profile, where ratios remain constant or decrease with depth.

Multichannel Analysis of Surface Rayleigh Waves (MAS_{RW}) V_S Model

MAS_{RW} shear wave velocities (V_S) range from approximately 270 m/s at the surface to approximately 950 m/s at depths of about 35 meters below the ground surface (fig. 14), the maximum imaged depth of the MAS_{RW} model. The MAS_{RW} model reveals two areas with distinct velocity characteristics, roughly defined by meters 0-175 (southwest), and meters 175-290 (northeast) along the seismic profile.

V_S values observed in the southwest (0-175 m) section of the seismic profile range from approximately 450-950 m/s. The velocity contour lines develop into a gently sloping concave-down feature, with a near-vertical axis centered at distance meter 40 along the profile, below 5 m. Northeast of distance meter 50 along the profile, velocity contours dip to the northeast. The velocity gradient of the southwest section averages from approximately 7-9 m/s per meter of depth.

V_S values observed in the northeast (175-290 m) section of the seismic profile range approximately 270-630 m/s. In the upper 10 m of the seismic profile, velocity contours dip near-vertically and abruptly change slope to near-horizontal to the northeast. Below 10 m depth, velocity contours are subparallel and near-horizontal. The velocity gradient of the northeast section averages approximately 6-9 m/s per meter of depth.

In general, observed V_S in the MAS_{RW} model are highest to the southwest and decrease to the northeast. Velocity contours in the southwest section trend generally concave, and in the northeast section, velocity contours dip to the east. Velocity gradients range from 6-9 m/s per meter of depth along the seismic profile.

Multichannel Analysis of Surface Love Waves (MAS_{LW}) V_S Model

MAS_{LW} shear wave velocities (V_S) range from approximately 150 m/s at the surface to approximately 1000 m/s at depths of about 27 meters below the ground surface (fig. 15). The maximum imaged depth of the MAS_{LW} model is approximately 30 m. The MAS_{LW} model reveals two areas with distinct velocity characteristics, roughly defined by meters 0-160 (southwest), and meters 160-290 (northeast) along the seismic profile.

V_S values observed in the southwest (0-160 m) section of the seismic profile range from approximately 400 to 1200 m/s. The velocity contour lines develop into a gently sloping concave-down feature with a near-vertical axis centered at distance meter 35 along the profile, below ~7 m depth. Northeast of distance meter 50 along the profile, velocity contours are subparallel and dip gently to the northeast. The velocity gradient of the southwest section averages approximately 16-23 m/s per meter of depth.

V_S values observed in the northeast (160-290 m) section of the seismic profile range between approximately 150-850 m/s. In the upper 6 m of the seismic profile, velocity contours dip near vertically, and abruptly change slope to near-horizontal to the northeast. Below 6 m depth, velocity contours are subparallel and near-horizontal to approximately 16 m depth, below which, the contours dip steeply to the northeast. The

velocity gradient of the northeast section averages approximately 11-12 m/s per meter of depth.

In general, observed V_S in the *MAS_LW* model are highest to the southwest and decrease to the northeast. Velocity contours in the southwest section form concave-down velocity contours; velocity contours dip gently to the northeast and steepen beginning at approximately distance meter 160 along the seismic profile. Velocity gradients range from 11-23 m/s per meter of depth along the seismic profile, decreasing from the southwest to the northeast.

DISCUSSION

Notable features seen in the P-wave tomography (fig. 6) include a low-velocity zone (LVZ) that dips roughly 50 degrees down to the northeast at approximately distance 150 m along the seismic profile. The LVZ defined by increasing (>2400 m/s) velocities immediately to the northeast and the southwest and decreasing (<2400 m/s) velocities above and immediately below the anomaly. In general, P-wave velocities tend to be lower to the northeast and higher to the southwest. The 1500 m/s velocity contour, which in previous studies by Catchings and others (1999a, 1999b; 2001, 2006, 2009, 2013, 2014, 2017) has been shown to coincide with the bottom of the vadose zone, shows that the top of ground water on the southwest side of the LVZ is up to 25 m higher than that on the northeast side. This result is not immediately intuitive as the overall gradient of the hilltop campus location slopes from east to west. Furthermore, the elevation of station 60 (163.2 m) at the northeast end of the seismic line is 1.5 m higher in elevation than station 1 (161.7 m) at the southeast end of the seismic line as seen in the GPS data (Table 2). Finally, groundwater level data from monitoring wells located about 13 km to the southeast of CSUEB near Quarry Lakes (Fig. 7) in Fremont show the water table to be about 8-9 m higher on the northeast side of the Hayward Fault than the southwest side at various times of the year (Table 3).

Faults can deflect the flow of groundwater near the surface as well as at depth (Fig. 8) (Alameda County Water District, 2017; Bense, 2006). Although the LVZ in the P-wave tomography is interpreted as fault containing saturated, crushed material, the presence of a fault does not seem to be the only factor affecting local water table

elevations. Rather, local topography and subsurface structure, specifically the filled, westward-sloping stream channel is channeling groundwater water away from the viewer into the plane of the page (toward NW) at the northeast section of the seismic line.

S-wave tomography (Fig. 9) shows a velocity contour pattern similar to the V_P model (Fig. 6), although muted. The LVZ visible at the center of the P-wave tomography model is expressed in the V_S model as a convex low-velocity anomaly that becomes steeper with depth, has higher V_S immediately to the northeast and to the southwest, and has a locally reduced-velocity gradient below.

The V_P/V_S and Poisson's ratio models (Figs. 12, 13) show a zone of high (>3.5 and >0.45 , respectively) values coincident with the LVZ seen in the V_P model and the anomalous low- V_S zone seen near the center of the line in the S-wave tomography (Fig. 9). The Poisson's Ratio value = 0.43 contour closely resembles the $V_P = 1500\text{m/s}$ contour (Figs. 13, 6), agreeing with past studies (Catchings et al., 2007, 2009; 2014), that show Poisson's Ratio values greater than 0.43 indicate the top of groundwater.

S-wave velocities in the MAS_{RW} and MAS_{LW} (Figs. 14, 15) models are consistent with the S-wave tomography, although the velocities are higher than those found in the V_S tomography model (Fig. 9). The LVZ seen in S-wave tomography appears at the upper 10 m between distance meter 110 and 175 for the MAS_{RW} model, and at the upper 5 m between distance meter 115 and 165 for the MAS_{LW} model. All three models also consistently show higher shear-wave velocities in the southwest and lower shear-wave velocities in the northeast. Overall, the $MAS_{R,LW}$ models have shallower depth of resolution (<35 m depth) than S-wave tomography (approximately 40 m depth).

The clear difference in magnitude of seismic velocities (higher to the southwest, lower to the northeast) and their ratios suggest a lateral change in subsurface geology (Fig. 16, 17); this change in velocity is seen in both P- and S-wave velocity models (Figs. 6, 9), as well as in their ratios (Figs. 12, 13). The higher velocity areas of the tomography models are consistent with the location of the gabbro unit of the SLB mapped on the 1:24,000 7.5-minute USGS Hayward quadrangle, whereas the lower velocities to the northeast are consistent with the shale and siltstone Knoxville formation mapped as the unit adjacent to the SLB to the northeast.

The LVZ seen in the P-wave tomography model, along with the low V_S , high V_P/V_S and Poisson's Ratio anomalies observed in the respective models (Figs. 6, 9, 12, 13) all fall approximately at the center of the seismic line, coincident with an abrupt lateral change in the depth to top of ground water, which suggest a groundwater barrier related to faulting (Bredehoeft et al., 1992; Caine and Forester, 1999; Catchings et al., 1999, 2009; Gandhok et al., 1999). These anomalies are common among the models and are consistent with low-velocity zones interpreted as sheared, groundwater-saturated rock material within a fault (Catchings et al., 2009, 2016; Gandhok et al., 1999; Rosa et al., 2016; Strayer et al., 2017). Furthermore, these anomalous structures dip moderately ($\sim 50^\circ$) to the east at shallow levels and correlate with the mapped trace of the WCF, at the center of the seismic array beneath Old Hillary Road (Fig. 3). The LVZ does not, however, appear to demarcate the boundary between the gabbroic SLB and the sedimentary rocks of the GVS (Fig. 2). Rather, the LVZ appears to be located within the high velocity gabbro, some 10 m to the southwest of the location where the velocity

contours become more uniform within what is interpreted as the Knoxville formation of the GVS, suggesting that the WCF in fact passes through the gabbro. This finding is not consistent with current geological maps, which depict the WCF as the contact between the gabbro and sandstone units. This interpretation relocates the WCF approximately 30 m to the southwest, to approximately distance meter 120 on the seismic line (Graymer, 2000).

CONCLUSIONS

Both P- and S-wave seismic velocity models show abrupt, steeply dipping velocity anomalies between distance meters 100 and 150 of the CSUEB campus West Chabot Fault seismic profile. The two zones of distinct velocities represent the high-velocity gabbro to the southwest and the lower-velocity Knoxville unit to the northeast. Furthermore, both the significant depth change to the top of ground water above the anomaly in the V_P model as well as the steeply eastward-dipping anomalies seen among the V_P , V_P/V_S , and Poisson's Ratio models are consistent with previous studies, suggesting that impermeable, steeply dipping, groundwater-saturated, faulted rock offsets the water table by up to 25 m (Figs. 6, 12, 13) (Bredehoeft et al., 1992; Caine and Forester, 1999; Catchings et al., 2009, 2016; Gandhok et al., 1999; Rosa et al., 2016; Strayer et al., 2017). However, although these observed differences in groundwater elevations were expected, local topography is likely the reason for the significant difference in groundwater conditions beneath the survey site. Finally, the steeply-dipping anomaly is framed by areas of similar high velocities, suggesting that the trace of the West Chabot Fault cuts through the San Leandro Block gabbro, not the GVS-SLB contact, as it crosses the CSUEB Hayward campus.

REFERENCES

- Aagaard, B.T., Blair, J.L., Boatwright, J., Garcia, S.H., Harris, R.A., Michael, A.J., Schwartz, D.P., and DiLeo, J.S., 2016, Earthquake outlook for the San Francisco Bay region 2014–2043 (ver. 1.1, August 2016): U.S. Geological Survey Fact Sheet 2016–3020, 6 p., <http://dx.doi.org/10.3133/fs20163020>.
- Abimbola, A.O., 2016, Seismic Imaging of Structures Between the Hayward and Chabot Faults at CSUEB [M.Sc. thesis]: California State University, East Bay, 80 p.
- Alameda County Water District, 2017, Final 2017 Groundwater Monitoring Report, Retrieved from <https://www.acwd.org/DocumentCenter/View/126>.
- Bense, V.F., Person, M.A., 2006, Faults as Conduit- Barrier Systems to Fluid Flow in Siliciclastic Sedimentary Aquifers: *Water Resources Research*, vol. 42, no. 5.
- Bredehoeft, J.D., Belitz, K., and Sharp-Hansen, S., 1992, The hydrodynamics of the Big Horn Basin: a study of the role of faults: *American Association of Petroleum Geologists Bulletin*, v. 76, p. 530–546.
- Burger, R.H., Sheehan, A.F., and Jones, C.H., 2006, *Introduction to Applied Geophysics*: New York, W.W. Norton and Company, Inc., 554 p.
- Caine, J. S. and Forester, C.B., 1999, Fault zone architecture and fluid flow: Insights from field data and numerical modeling, in *Faults and Subsurface Fluid Flow in the Shallow Crust*, in Haneberg, W.C., Mozley, P.S., Moore, J.C., and Goodwin, L.B., eds., *Geophysical Monograph Series*: Washington, D. C., American Geophysical Monograph, v. 113, p. 101–127.

- California Department of Transportation, 2018, Caltrans Geotechnical Manual, retrieved from http://www.dot.ca.gov/hq/esc/geotech/geo_manual/manual.html.
- California Geological Society, 2018, Earthquake Fault Zones: A Guide for Government Agencies, Property owners/Developers, and Geoscience Practitioners for Assessing Fault Rupture Hazards in California, Special Publication 42.
- Case, J.E., 1968, Upper Cretaceous and Lower Tertiary Rocks, Berkeley and San Leandro Hills, California: Contributions to General Geology, Geological Survey Bulletin 1251-J.
- Castagna, J.P., Batzle, M.L., and Eastwood, R.L., 1985, Relationships between compressional-wave and shear-wave velocities in clastic silicate rocks: Geophysics, v. 50, p. 571–581.
- Catchings, R. D., Goldman, M.R., Gandhok, G., Horta, E., Rymer, M.J., Martin, P., and Christensen, A., 1999, Structure, Velocities, and Faulting Relationships Beneath San Geronio Pass, California: Implications for Water Resources and Earthquake Hazards, US Geological Survey Open-File Report 99-568, 53 pp.
- Catchings, R. D., Gandhok, G., Goldman, M. R., and Okaya, D., 2001, Seismic images and fault relations of the Santa Monica Thrust Fault, West Los Angeles, California: U.S. Geological Survey Open-File Report 01-111, 34 pp., <https://pubs.usgs.gov/of/2001/0111/>.
- Catchings, R.D., Borchers, J.W., Goldman, M.R., Gandhok, G., Ponce, D.A., and Steedman, C.E., 2006, Subsurface structure of the East Bay plain ground-water basin: San Francisco Bay to the Hayward Fault, Alameda County, California: U.S.

Geological Survey Open-File Report 2006-1084, 61 p.,

<https://pubs.usgs.gov/of/2006/1084/>.

Catchings, R.D., Gandhok, G., Goldman, M.R., and Steedman, C., 2007, Near-surface structure and velocities of the northeastern Santa Cruz Mountains and the western Santa Clara Valley, California, from seismic imaging: U. S. Geological Survey Open-File Report 2007–1039.

Catchings, R.D., Rymer, M.J., Goldman, M.R., and Gandhok, G., 2009, San Andreas Fault geometry at Desert Hot Springs, California, and its effects on earthquake hazards and groundwater: Bulletin of the Seismological Society of America, v. 99, no. 4, pp. 2190-2207.

Catchings, R.D., Rymer, M.J., Goldman, M.R., Prentice, C.S., and Sickler, R.R., 2013, Fine-scale delineation of the location of and relative ground shaking within the San Andreas Fault zone at San Andreas Lake, San Mateo County, California: U.S. Geological Survey Open-File Report 2013–1041, 53 p.,
<http://pubs.usgs.gov/of/2013/1041/>.

Catchings, R.R., Rymer, M.J., Goldman, M.R., Sickler, R.R., and Criley, C.J., 2014, A method and example of seismically imaging near-surface fault zones in geologically complex areas using V_p , V_s , and their ratios, Bulletin of the Seismological Society of America, v. 104, p. 1989-2006.

Catchings, R.D., Strayer, L.M., Goldman, M.R., Criley, C.J., Garcia, S.H., Sickler, R.R., Catchings, M.K., Chan, J.H., Gordon, L., Haefner, S., Blair, L., Gandhok, G., and Johnson, M., 2015, 2013 East Bay Seismic Experiment (EBSE) -- Implosion Data,

Hayward, Calif: U.S. Geological Survey data release,

<http://dx.doi.org/10.5066/F7BR8Q75>.

Catchings, R.D., Goldman, M.R., Li, Y.-G., and Chan, J.H., 2016, Continuity of the West

Napa–Franklin Fault Zone Inferred from Guided Waves Generated by Earthquakes

Following the 24 August 2014 M w 6.0 South Napa Earthquake: Bulletin of the

Seismological Society of America, v. 106, p. 2721–2746.

Catchings, R.D., Goldman, M.R., Trench, David, Buga, Michael, Chan, J.H., Criley, C.J.,

and Strayer, L.M., 2017, Shallow-depth location and geometry of the Piedmont

Reverse splay of the Hayward Fault, Oakland, California: U.S. Geological Survey

Open-File Report 2016–1123, 22 p., <https://pubs.usgs.gov/of/2016/1123/>.

Dobrin, M.B., 1960, Introduction to Geophysical Prospecting: New York, McGraw Hill,

867 p.

Ferriz, H., Hayashi, K., Sandhu, R., Loogman, A., 2016, Geophysical Investigation of

Flood Control Levees in the Sacramento-San Joaquín Estuary, California: Applied

Geology in California, p. 283-299.

Fusee, R., Bednarz, S., 2016, The New Irvington Tunnel Excavation and Geologic

Documentation: Applied Geology in California, p. 29-50.

Gandhok, G., Catchings, R.D., Goldman, M.R., Horta, E., Rymer, M.J., Martin, P., and

Christensen, A., 1999, High-Resolution Seismic Reflection/Refraction Imaging

from Interstate 10 to Cherry Valley Boulevard, Cherry Valley, Riverside County,

California: Implications for Water Resources and Earthquake Hazards, US

Geological Survey Open-File Report 99-320, 52 pp.

- Graymer, R.W., 1995, Geology of the Southeast San Francisco Bay Area Hills, California, *in* Recent Geologic Studies in the San Francisco Bay Area: Pacific Section of the Society of Economic Paleontologists and Mineralogists, p. 115-124.
- Graymer, R.W., 2000, Geologic map and map database of the Oakland metropolitan area, Alameda, Contra Costa, and San Francisco Counties, California: U.S. Geological Survey Miscellaneous Field Studies MF-2342, scale 1:50,000, <https://pubs.usgs.gov/mf/2000/2342/>.
- Gregory, A.R., 1976, Fluid Saturation Effects on Dynamic Elastic Properties of Sedimentary Rocks: *Geophysics*, v. 41, p. 895–921.
- Hayashi, K., and Hikima, K., 2003, CMP analysis of multi-channel surface wave data and its application to near-surface S-wave velocity delineation, *in* 16th EEGS Symposium on the Application of Geophysics to Engineering and Environmental Problems, p. 1348–1355.
- Hayashi, K., and Suzuki, H., 2004, CMP cross-correlation analysis of multi-channel surface-wave data: *Exploration Geophysics*, v. 35, p. 7–13.
- Hayashi, K., Cakir, R., and Walsh, T.J., 2016, Comparison of dispersion curves and velocity models obtained by active and passive surface wave methods: *Society of Exploration Geophysicist Technical Program Expanded Abstracts 2016*, p. 4983-4988, <https://doi.org/10.1190/segam2016-13846390.1>.
- Hole, J.A., 1992, Nonlinear high-resolution three-dimensional seismic travel time tomography: *Journal of Geophysical Research: Solid Earth*, v. 97, p. 6553–6562.

- Ivanov, J., Miller, R.D., Park, C.P., and Ryden, N., 2003, Seismic search for underground anomalies, *in* Society of Exploration Geophysicists Technical Program, p. 1223–1226.
- Ivanov, J., Leitner, B., Shefchik, W., Schwenk, J.T., and Peterie, S.L., 2013, Evaluating hazards at salt cavern sites using multichannel analysis of surface waves: The Leading Edge, v. 32, p. 298–305.
- Jones, D.L., and Graymer, R.W., 1993, Tectonics of the Mission - Chabot Faults: Annual Technical Report/Final Technical Report: Department of Geology and Geophysics, University of California, Berkeley.
- Keller, G.V., 1979, Resistivity Surveys and Engineering Problems: Geophysical Methods in Geotechnical Engineering. American Society of Civil Engineers National Convention, p. 1-50.
- McCalpin, J., 1996, Paleoseismology, Academic Press.
- McEvelly, T. V., and Johnson, L. R., 1974, Stability of P and S velocities from Central California quarry blasts: Bulletin of the Seismological Society of America v. 64, p. 343-353.
- Oakeshott, G.B., 1982, Hayward Fault Zone and a Western Outlier of the Coast Range Thrust in the Montclair District of Oakland, California: California Division of Mines and Geology Special Publication, v. 62, p. 55–64.
- Park, C.B., Miller, R.D., and Xia, J., 1997, Multi-Channel Analysis of Surface Waves (MASW): Geophysics, v. 64, p. 800–808.

- Park, C., Miller, R., and Xia, J., 1999, Multichannel analysis of surface waves: *Geophysics*, v. 64, no. 3, p. 800-808.
- Park, C., Miller, R., Xia, J., and Ivanov, J., 2000, Multichannel analysis of surface waves (MASW)—active and passive methods: *The Leading Edge*, v. 26, p. 60–64, doi: 10.1190/1.2431832.
- Park, C., 2013, MASW for geotechnical site investigation: *The Leading Edge*, v. 32, p. 656–662.
- Ponce, D.A., Hildenbrand, T.G., and Jachens, R.C., 2003, Gravity and magnetic expression of the San Leandro gabbro with implications for the geometry and evolution of the Hayward Fault Zone, northern California: *Bulletin of the Seismological Society of America*, v. 93, p. 14–26.
- Pujol, J., 2003, *Elastic Wave Propagation and Generation in Seismology*: Cambridge University Press, 462 p.
- Radbruch, D.H., 1969, Areal and engineering geology of the Oakland East quadrangle, California: U.S. Geological Survey Map GQ-769, 1:24,000 scale.
- Redpath, B.B., 1973, *Seismic refraction exploration for engineering site investigations*: Explosive Excavation Research Laboratory Livermore, California, Technical Report E-73-4, 52 p.
- Reynolds, J.M., 2011, *An Introduction to Applied and Environmental Geophysics*: West Sussex, UK, Wiley and Sons, Ltd., 696 p.
- Robinson, G.D., 1956, *Geology of the Hayward Quadrangle, California*: U.S. Geological Survey Miscellaneous Geological Quadrangle Map.

- Rosa, C.M., Catchings, R.D., Rymer, M.J., Grove, K., and Goldman, M.R., 2016, Structure of the 1906 near-surface rupture zone of the San Andreas Fault, San Francisco Peninsula segment, near Woodside, California: U. S. Geological Survey Open-File Report 2016–1063.
- Saari K., 1988, The Rock Engineering Alternative, Finnish Tunneling Association. 1988.
- Sharma, P. V., 1986. Geophysical Methods in Geology: New York, Elsevier Science Publishing Co., Inc., 442 p.
- Strayer, L. M., Catchings, R. D., McEvelly, A. T., Chan, J. H., Goldman, M. R., Criley, C. J., Richardson, I., and Sickler, R. R., 2017, The 2016 East Bay Seismic Investigation: Seismic Tomography Imaging across the Hayward Fault Zone near San Leandro, California, SSA 2017 Annual Meeting Announcement and Program. *Seismological Research Letters*; 88 (2B): 463–723, doi: <https://doi.org/10.1785/0220170035>.
- Tatham, R. H., 1982, V_P/V_S and lithology: *Geophysics*, v. 47, no. 3, 336-344.
- Thomsen, L., 1990, Poisson was not a geophysicist!: *The Leading Edge*, v. 9, p. 27-29.
- Uhlemann, S., Hagedorn, S., Dashwood, B., Maurer, H., Gunn, D., Dijkstra, T., and Chambers, J., 2016, Landslide Characterization Using P-and S-wave Seismic Refraction Tomography—the Importance of Elastic Moduli: *Journal of Applied Geophysics*, v. 134, p. 64–76.
- Waltham T., 2009, *Foundations of Engineering Geology* 3e, Spon Press.
- Xia, J., Miller, R.D., Park, C.B., Hunter, J.A., and Harris, J.B., 2000, Comparing shear-wave velocity profiles from MASW with borehole measurements in unconsolidated

sediments, Fraser River Delta, BC, Canada: *Journal of Environmental & Engineering Geophysics*, v. 5, p. 1–13.

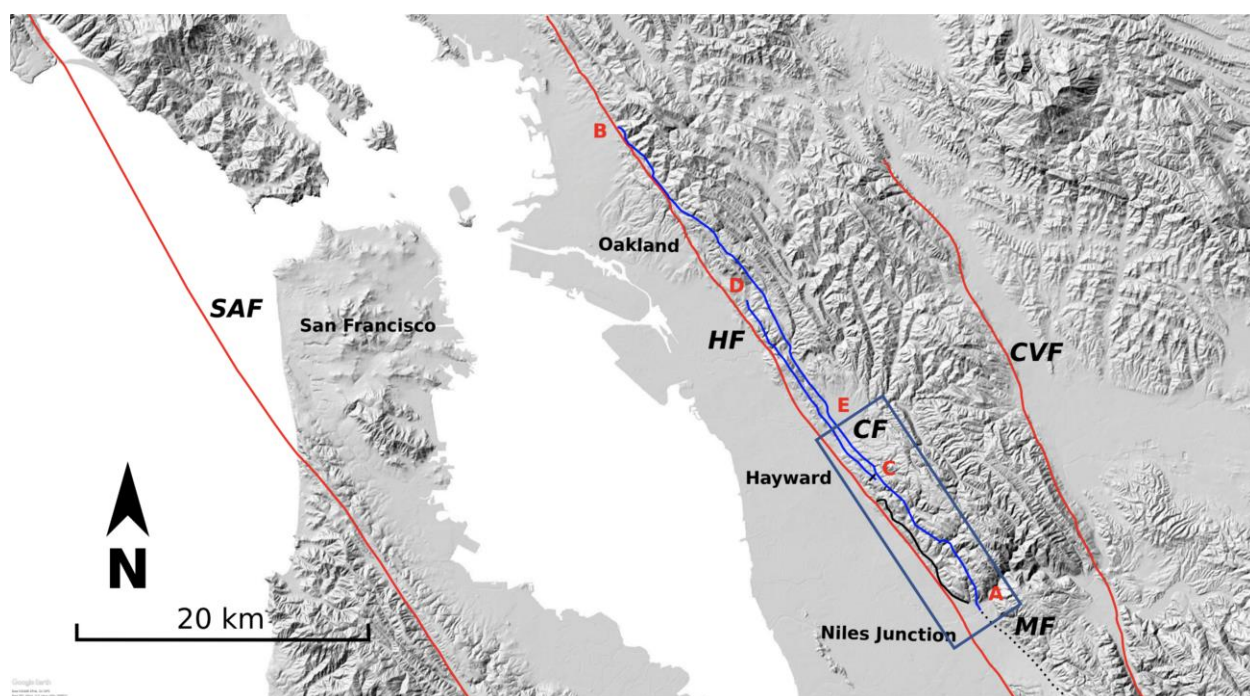


Figure 1: Regional map of San Francisco Bay Area. Historically active faults include: San Andreas Fault (SAF), Calaveras Fault (CVF), and Hayward Fault (HF); the West and East Chabot Faults (collectively, CF) are at least Pleistocene-active (Graymer, 2000). The southeastern extent of the ECF (blue) is at Niles Junction (A), where the ECF merges with the Mission Fault (black). The northwestern mapped extent of the ECF is near the University of California Memorial Stadium in Berkeley (B). The location of the 2015 seismic array is indicated by a black line (not to scale) crossing the WCF (blue) near its southeastern mapped extent on the CSUEB Hayward campus (C). The northwestern mapped extent of the WCF is near Merritt College in Oakland (D). Also marked are the approximate locations of the Great Valley Sequence-Coast Range Ophiolite contacts observed at Montera Middle School in Oakland by Oakeshott (1980) (E), and locations within the area covered by the USGS Hayward 7.5-minute Quadrangle (which includes the CSUEB study area plus the approximately 11km northwest upstrike of the CFS) by Graymer in 2000 (E). Blue rectangle indicates area represented in figure 2.

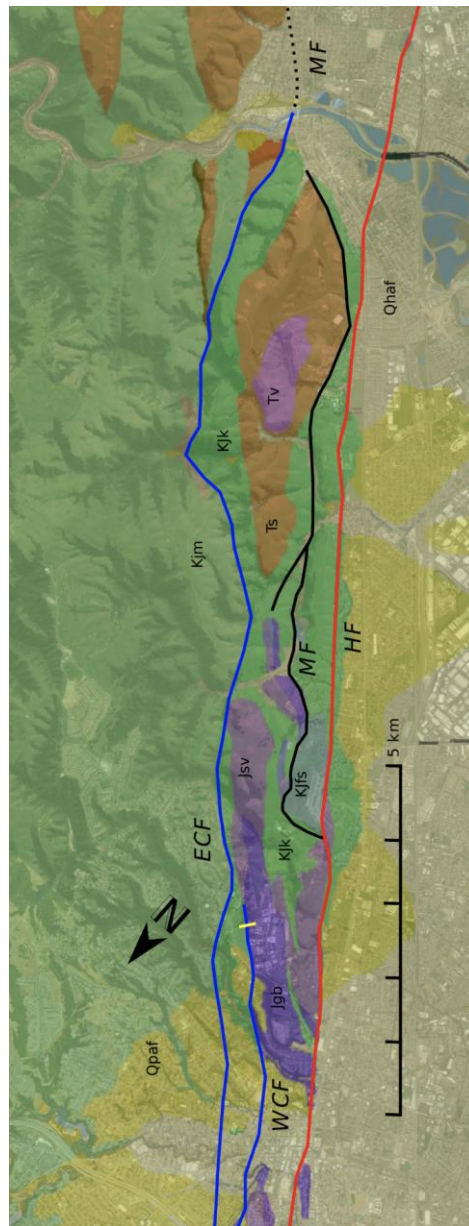


Figure 2: 2015 CSUEB West Chabot seismic investigation local geology. Seismic profile, 295 m in length, scaled, is indicated by yellow line, center left of map. Between the HF and ECF-MF, Jurassic-aged Coast Range Ophiolite units (Jgb, gabbro; Jsv, volcanics) and J-K aged Franciscan sandstone (KJfs) interfinger with the J-K aged Knoxville sandstone (KJk); K-aged Joaquin Miller sandstone (Kjm) and younger units of the Great Valley Sequence lie northeast of the ECF-MF. Tertiary sedimentary and volcanic units (Ts, Tv) lie to the north and east of the HF. Holocene- and Pleistocene-aged alluvial fan deposits (Qhaf, Qpaf) lie in topographic lows and southeast of the HF (modified from Quaternary fault and fold database for the United States: <https://earthquake.usgs.gov/hazards/qfaults/>, Graymer, 2000)

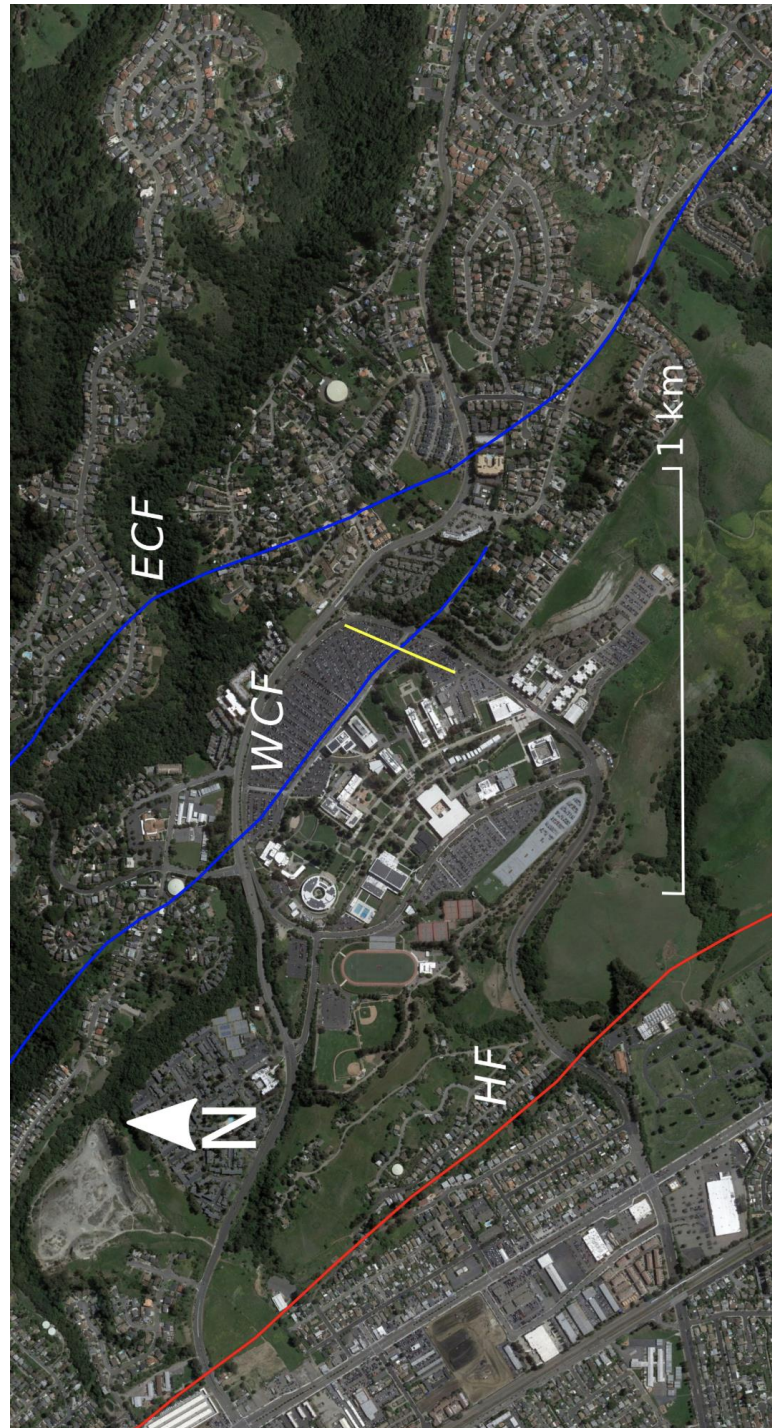


Figure 3: Local tectonics, CSUEB Hayward campus. Seismic profile, 295 m in length, to scale and is indicated by a yellow line. Hayward Fault indicated by red line, West and East Chabot Faults indicated by blue lines (modified from Google Earth satellite image).

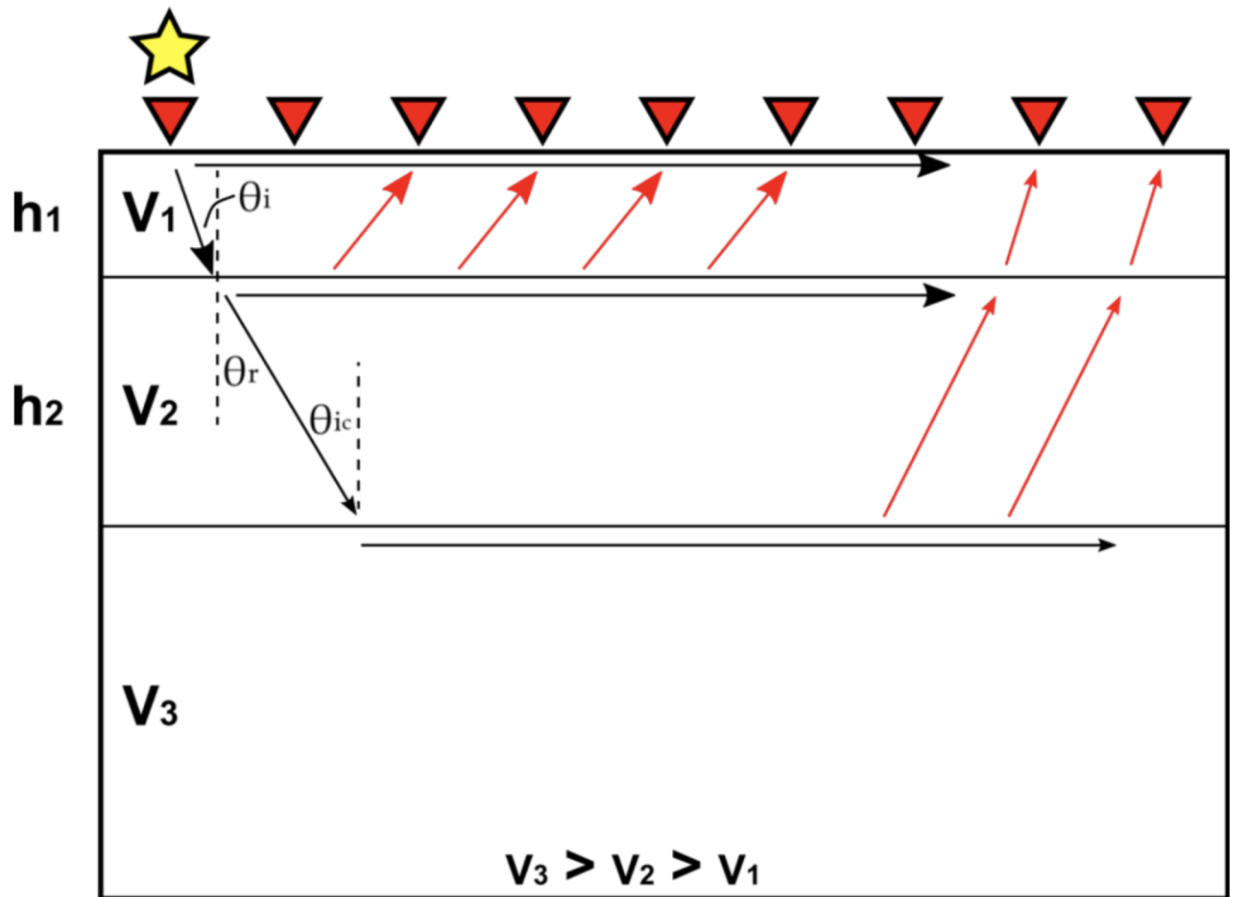


Figure 4: The illustration shows an example of a seismic wave generated by a near-surface active source (yellow star). Refracted waves travel horizontally in the subsurface at each interface (surface and V_1 , V_1 and V_2 , V_2 and V_3), serving as a point source for waves refracted in all directions, including back to the surface (θ_{ic}) where they are detected by the geophone sensors (red triangles) on the surface.

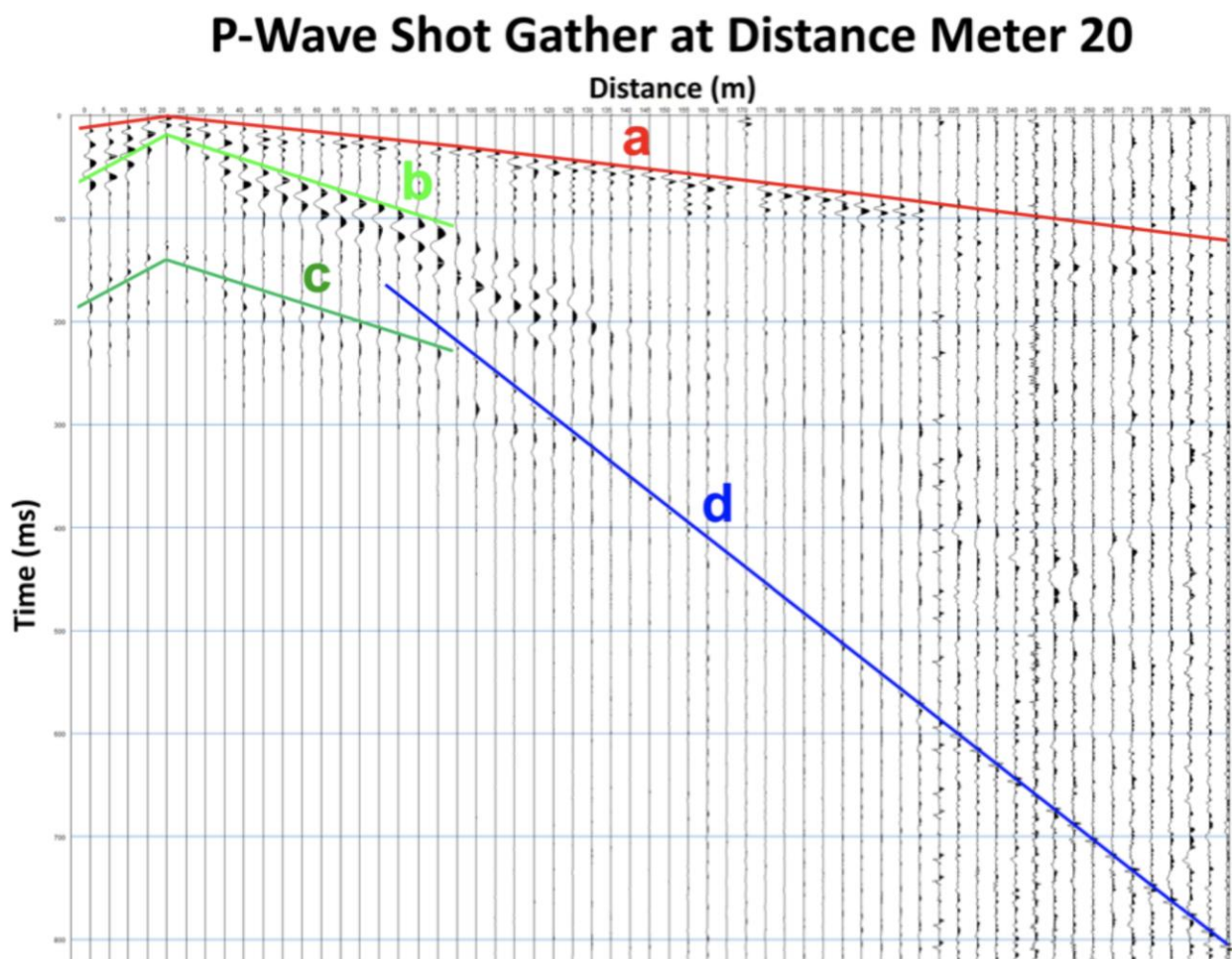


Figure 5: P-wave shot gather at distance meter 20. Upper horizontal axis shows distance in meters relative to geophone 1 (0 m). Left vertical axis shows signal travel time in milliseconds (ms). First-arrival refractions (a), Rayleigh (surface waves) (b), a multiple signal likely due to shot plate bounce (c), and an air wave travelling at approximately 330 m/s are shown by lines of various colors.

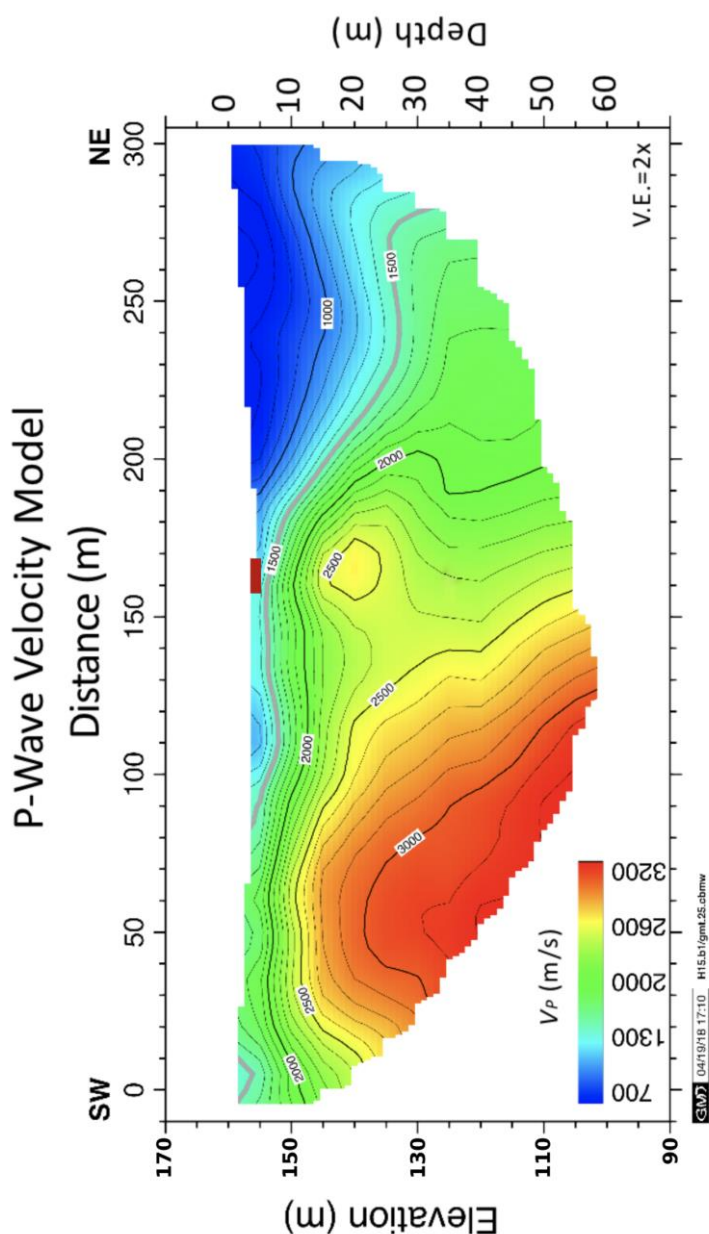


Figure 6: P-wave refraction velocity model for the 2015 West Chabot Fault seismic investigation. Upper horizontal axis shows distance in meters relative from geophone 1 (0 m). Left vertical axis shows elevation in meters relative to mean sea level. Right vertical axis shows approximate depth in meters. Old Hillary Road is indicated by a red bar at approximately distance meter 160; the mapped trace of the West Chabot Fault is located near the center of the line (150 m). Range of V_P is 600 to 3200 m/s. A steeply east-dipping low velocity zone is located near distance meter 130 m at a depth of approximately 15 m; similar features are seen in both the V_P/V_S and Poisson's Ratio models (Figs. 12 & 13). The 1500 m/s velocity contour is outlined in grey, indicating the top of groundwater.

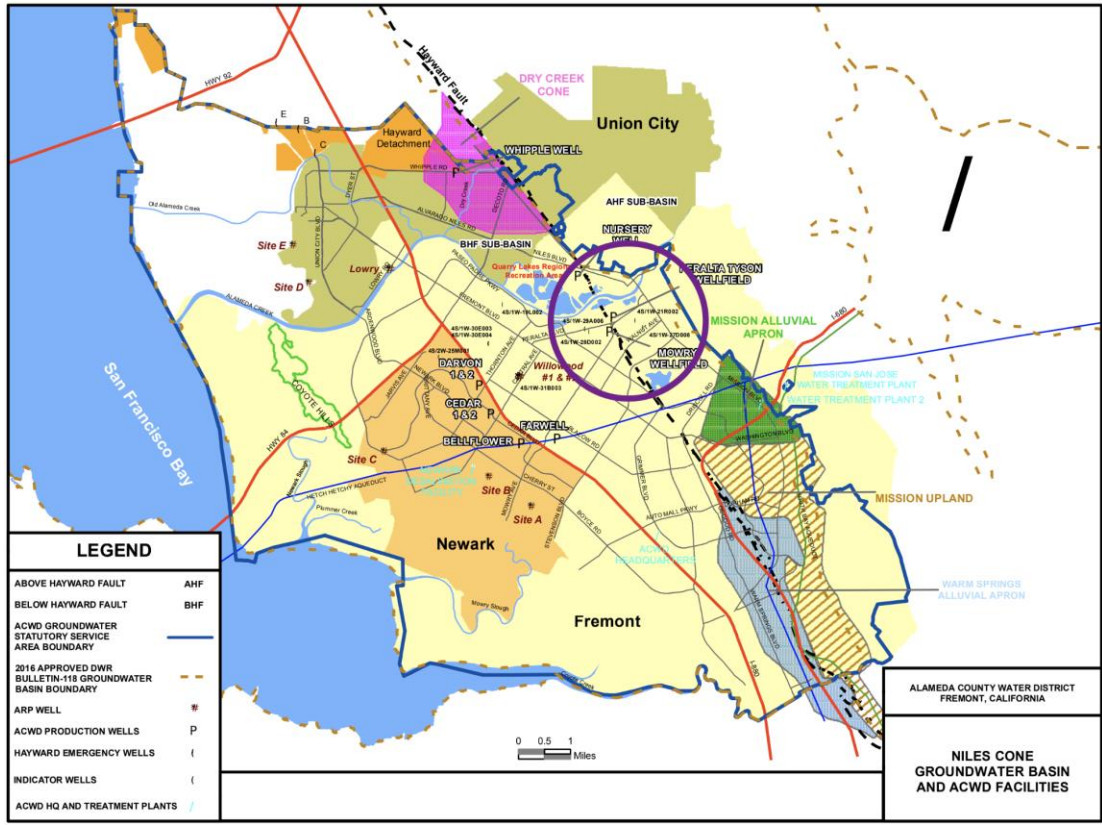


Figure 7: Map of ACWD facilities and monitoring stations near Niles Canyon. Of the four wells within the purple circle, well 4S/1W-27D008 to the northeast of the HF and well 4S/1W-29A006 had data available for March and September of 2017. Groundwater levels were consistently higher on the northeast side of the HF: 8.96 m in March and 7.95 m in September of 2017. There was no available data for wells 4S/1W-21R002 or 4S/1W-28D002. From Alameda County Water District Final 2017 Groundwater Monitoring Report.

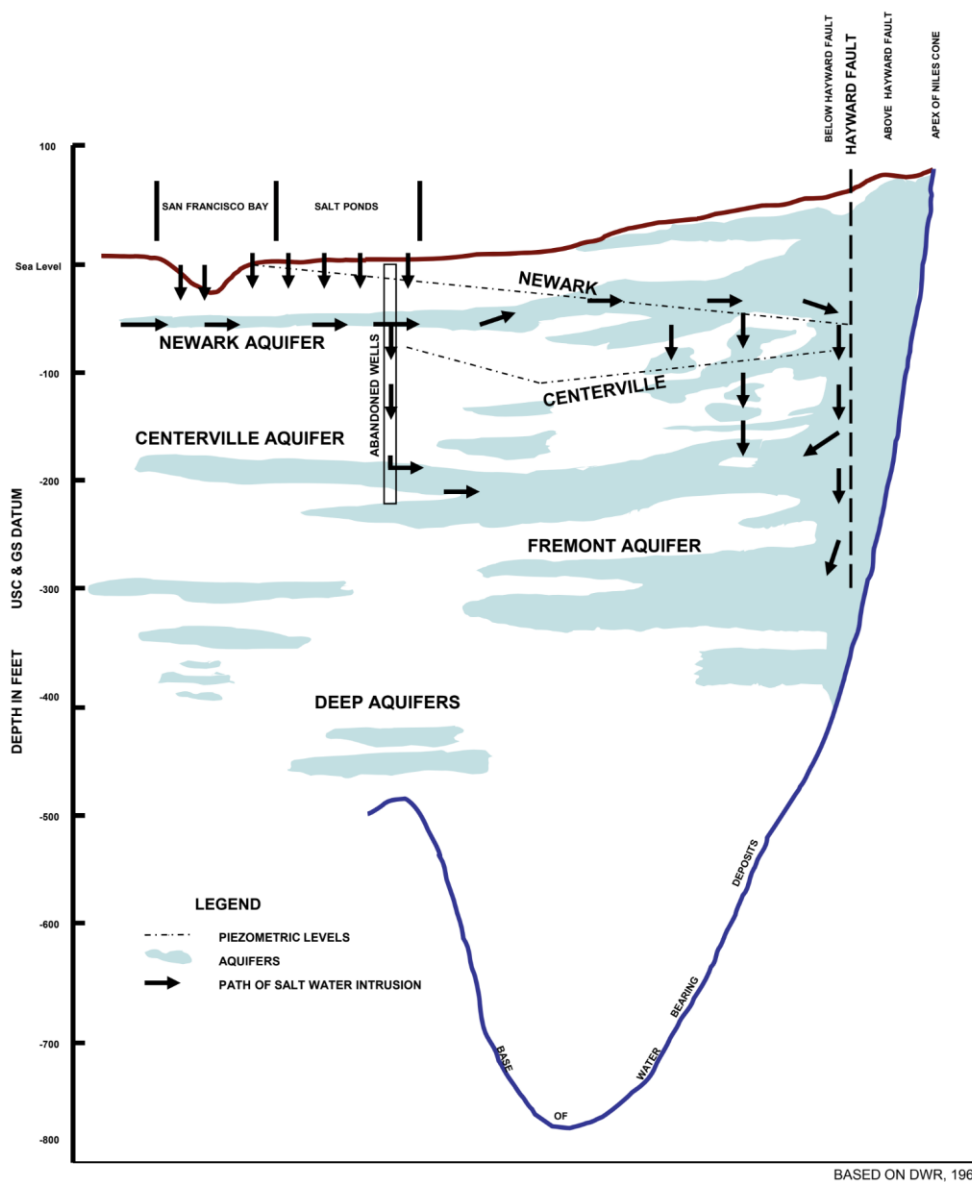


Figure 8: Examples of groundwater deflection by the Hayward Fault near Niles Canyon, Fremont, California. From Alameda County Water District Final 2017 Groundwater Monitoring Report.

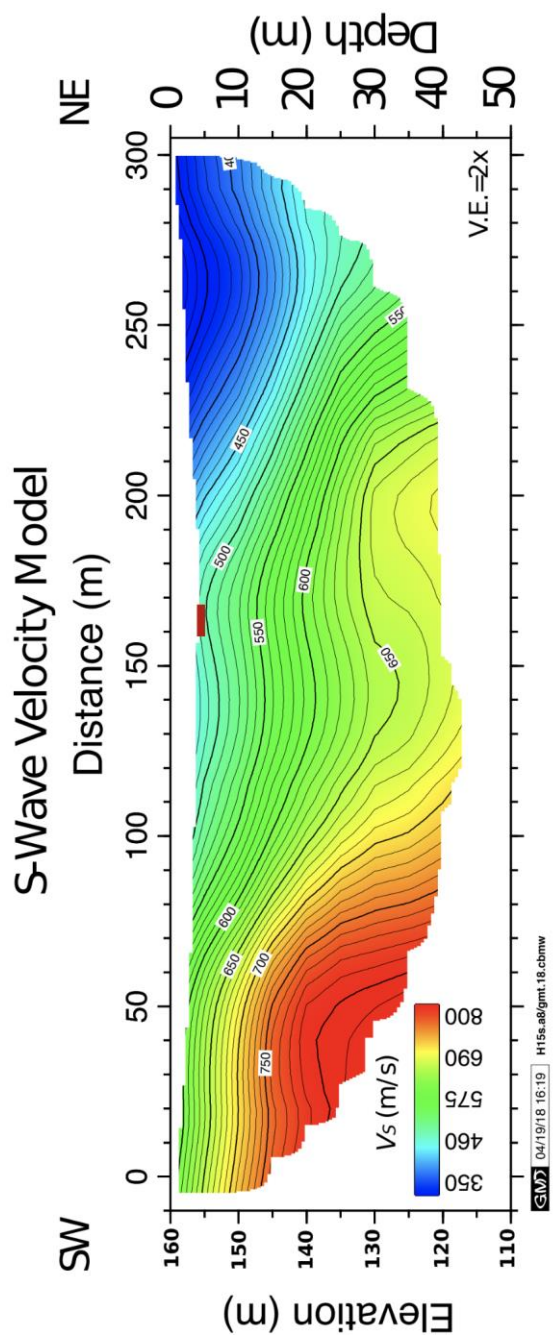


Figure 9: S-wave refraction velocity model for the 2015 West Chabot Fault seismic investigation. Upper horizontal axis shows distance in meters relative from geophone 1 (0 m). Left vertical axis shows elevation relative to mean sea level. Right vertical axis shows approximate depth. Old Hillary Road is indicated by a red bar at approximately distance meter 160; the mapped trace of the West Chabot Fault is located near the center of the line (150 m). Range of V_s is 330 to 800 m/s. Higher V_s is seen at the southwest end of the profile.

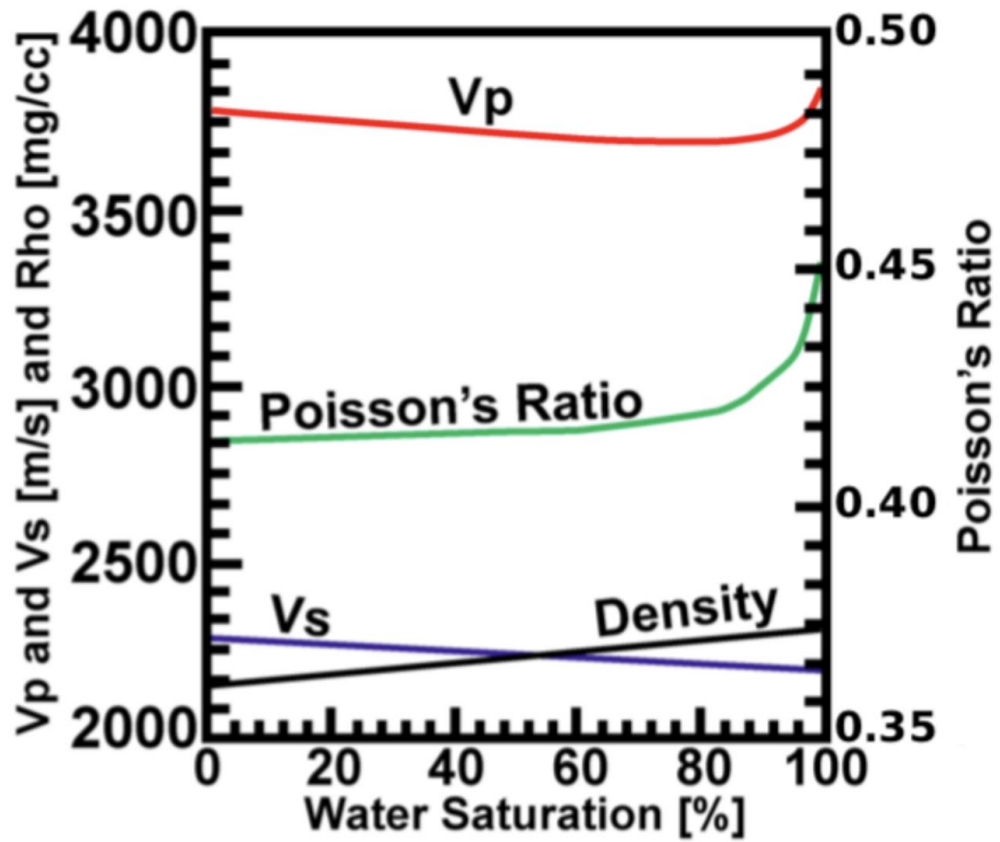


Figure 10: Changes in V_p , V_s (m/s), density (mg/cc), and Poisson's ratio with respect to percent water saturation.

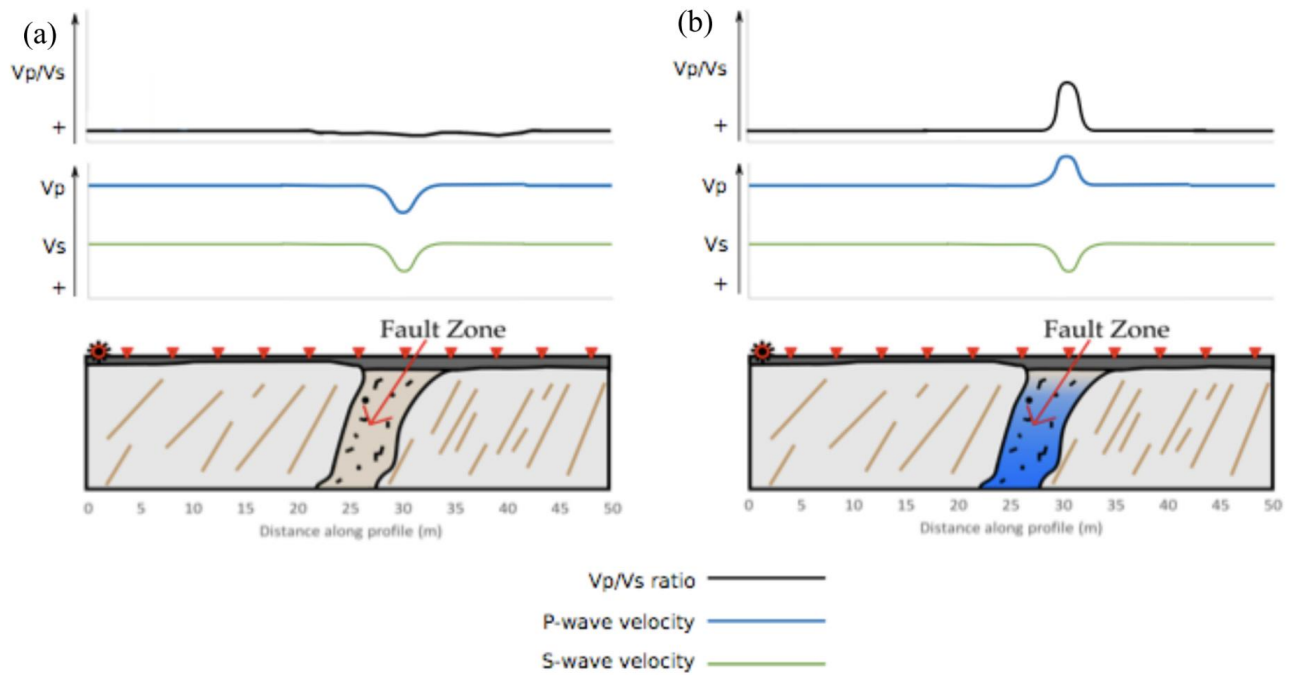


Figure 11: Simplified example showing the influence of groundwater saturation in faulted rock on P- and S-wave velocities and their ratios. V_p/V_s , V_p , and V_s values are indicated by black, blue, and green curves, respectively, with relative values indicated by the y-axes, positive in the up direction. (a) Unsaturated (<90%) fault scenario. V_p and V_s values decrease slightly within the fault material; V_p/V_s ratio largely unaffected. (b) Saturated fault scenario. V_p increases sharply within the fault zone, V_s remains largely unaffected. V_p/V_s values increase sharply within the faulted material. Modified from Abimbola (2016).

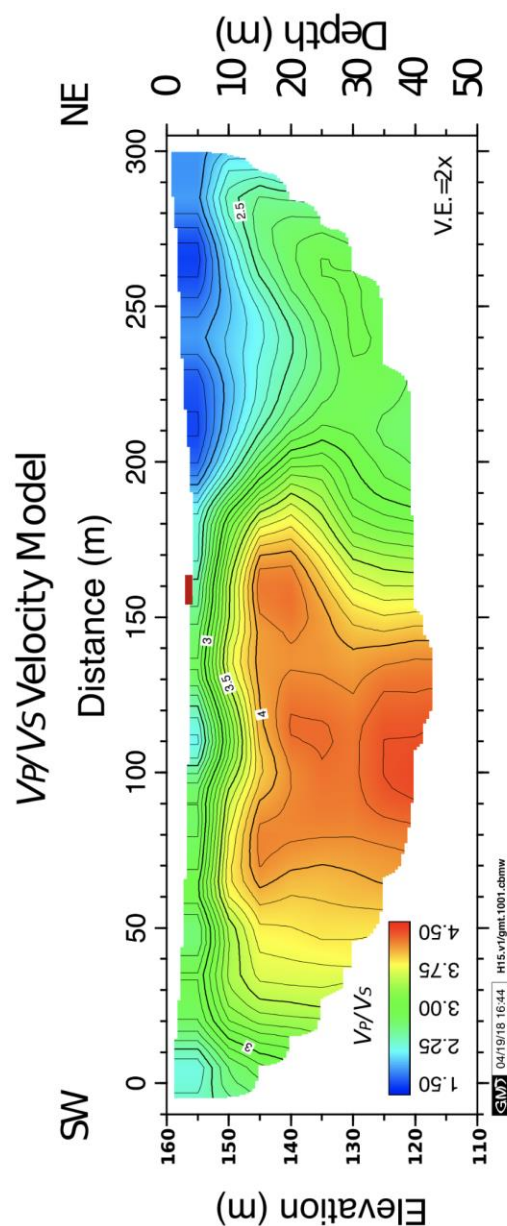


Figure 12: V_P/V_S ratio model for the 2015 West Chabot fault seismic investigation. Upper horizontal axis shows distance in meters relative from geophone 1 (0 m). Left vertical axis shows elevation in meters relative to mean sea level. Right vertical axis shows approximate depth in meters. Old Hillary Road is indicated by a red bar at approximately distance meter 160; the mapped trace of the West Chabot Fault is located near the center of the seismic line (150 m). Range of V_P/V_S is 1.7 to 4.4. The highest V_P/V_S values are between distance meters 30-190 along the seismic profile. High (>3.5) V_P/V_S values surround a steeply-dipping area of slightly lower V_P/V_S near distance meter 130 m at a depth of approximately 15 m; similar features are seen in both the V_P and Poisson's Ratio models, (Figs. 6 & 13)

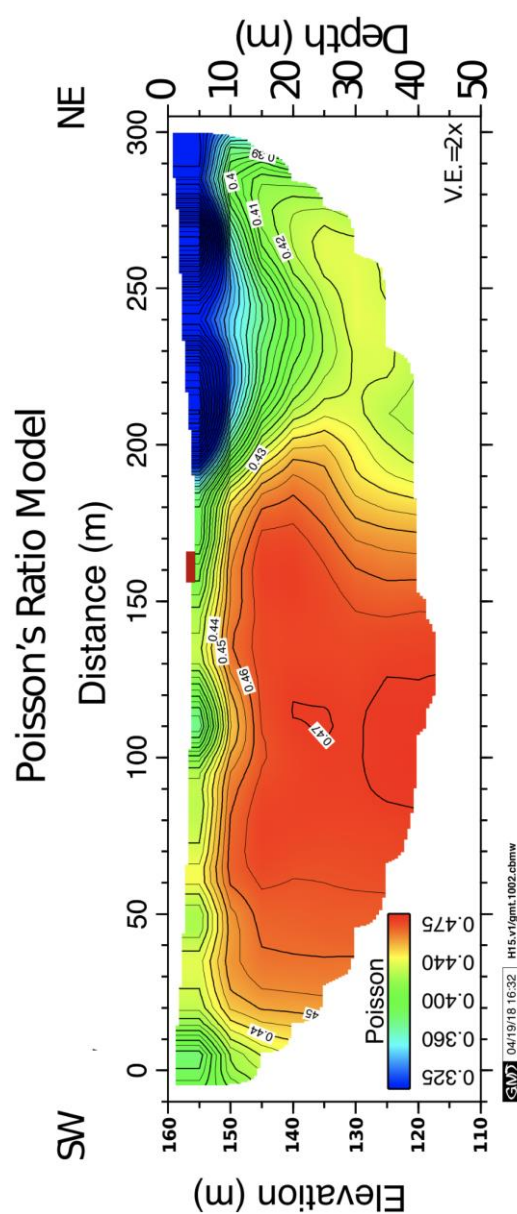


Figure 13: Poisson's ratio model for the 2015 West Chabot Fault seismic investigation. Upper horizontal axis shows distance in meters relative from geophone 1 (0 m). Left vertical axis shows elevation in meters relative to mean sea level. Right vertical axis shows approximate depth in meters. Old Hillary Road is indicated by a red bar at approximately meter 160; the mapped trace of the West Chabot Fault is located near the center of the seismic line (150 m). Poisson's ratios range from 0.30 to 0.47. The highest Poisson's ratios are between meters 50 and 170 along the seismic profiles: high (> 0.425) Poisson's ratio values indicate water-saturated material. Velocity contours at about distance meter 140 dip steeply to the east, similar to features seen in both V_p and V_p/V_s models (Figs. 6 & 12).

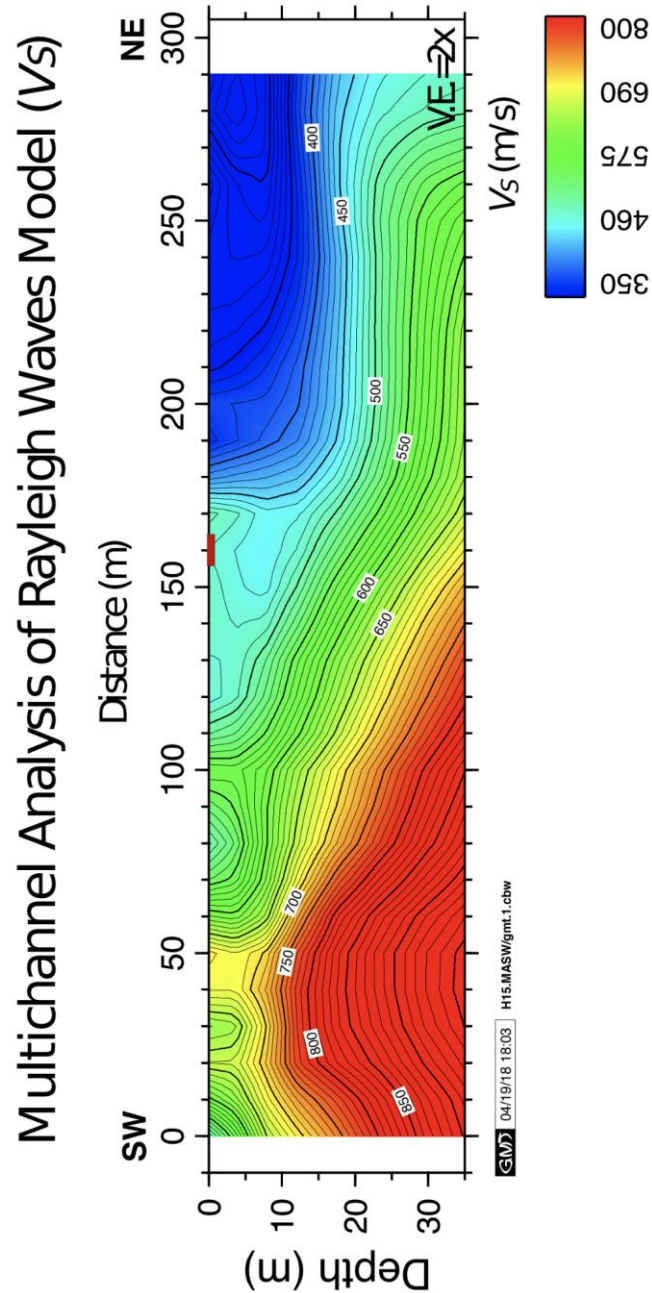


Figure 14: MAS_RW velocity model for the 2015 West Chabot Fault seismic investigation. Upper horizontal axis shows distance in meters relative from geophone 1 (0 m). Left vertical axis shows approximate depth in meters. Vertical exaggeration is 2x. Old Hillary Road is indicated by a red bar at approximately distance meter 160. The mapped trace of the West Chabot Fault is near the center of the seismic line (150 m). V_s ranges from 270 to 950 m/s. The highest V_s are seen at the southwest end of the seismic profile.

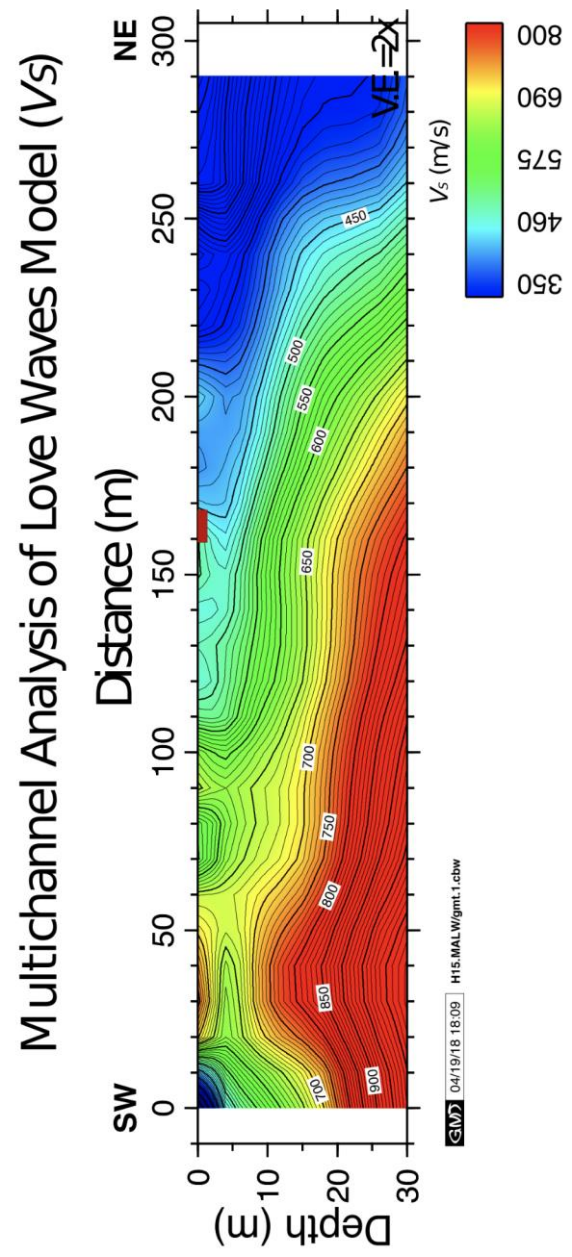


Figure 15: MAS_LW velocity model for the 2015 West Chabot Fault seismic investigation. Upper horizontal axis shows distance in meters relative from geophone 1 (0 m). Left vertical axis shows approximate depth in meters. Vertical exaggeration is 2x. Old Hillary Road is indicated by a red bar at approximately distance meter 160; the mapped trace of the West Chabot Fault is located near the center of the seismic line (150 m). V_s ranges from 150 to 1000 m/s. The highest V_s are seen at the southwest end of the seismic profile.

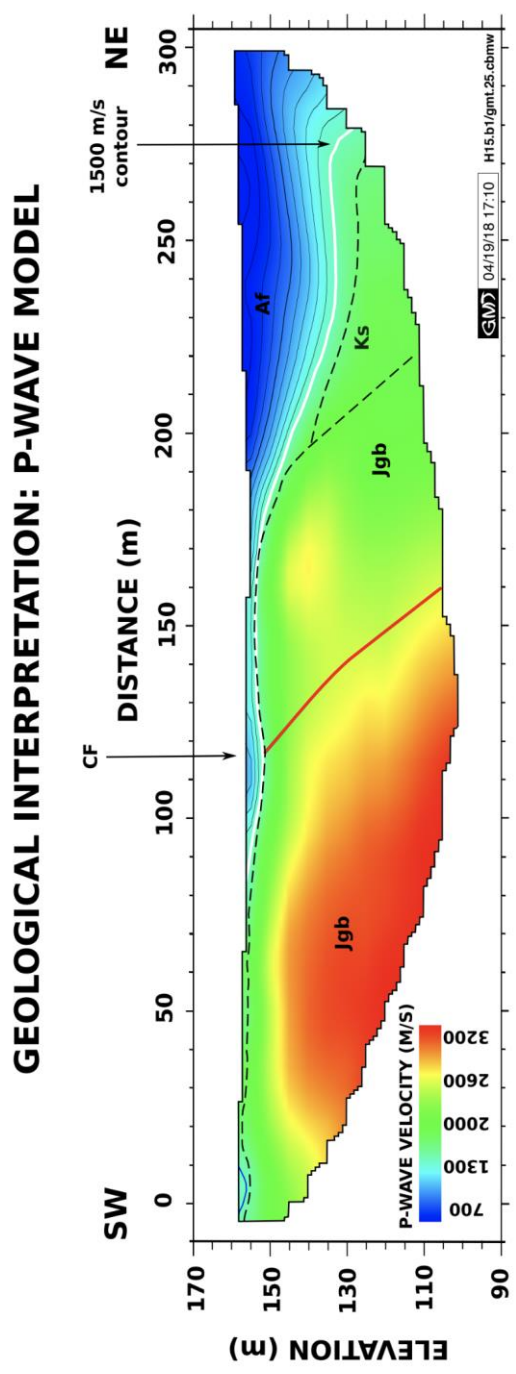


Figure 16: Subsurface geology model, V_p tomography shown. Model is interpreted based on P-wave velocities determined by the 2015 Chabot Fault seismic investigation, areal imagery and geologic maps, and field observations. The $V_p = 1500$ m/s contour, in white, indicates the top of groundwater. The interpreted location of the Chabot Fault is traced in red. The local gradient of the buried stream channel that passes below the seismic line near distance meter 230 dips down and toward the west

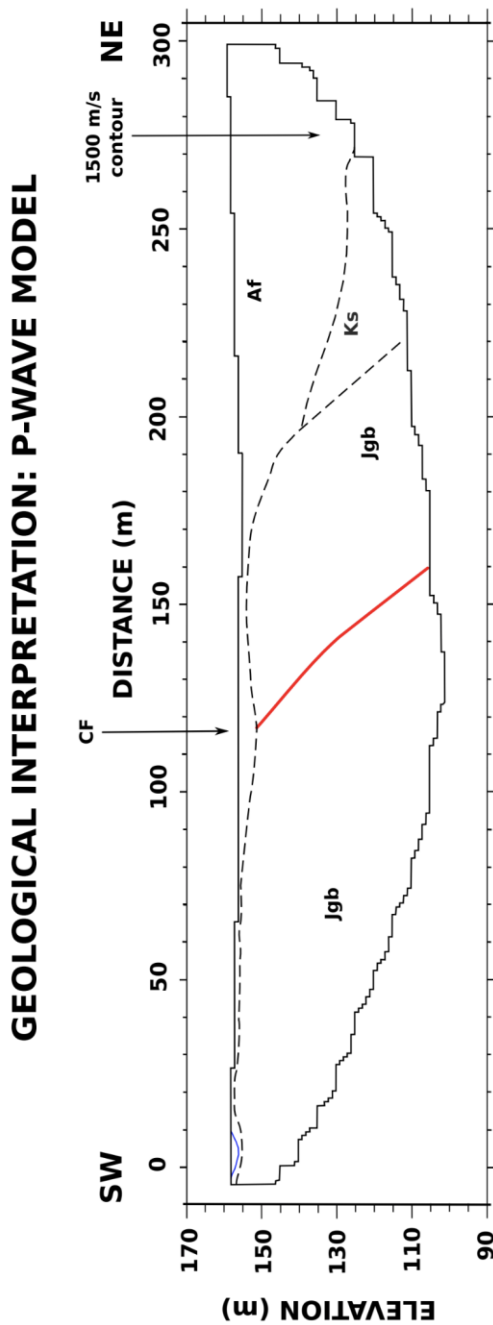


Figure 17: Subsurface geology model. Model is interpreted based on P-wave velocities determined by the 2015 Chabot Fault seismic investigation, areal imagery and geologic maps, and field observations. The $V_p = 1500$ m/s contour, in white, indicates the top of groundwater. The interpreted location of the Chabot Fault is traced in red. The local gradient of the buried stream channel that passes below the seismic line near distance meter 230 dips down and toward the west.

Table 1: P and S-wave acquisition and processing parameters.

P-wave dataset information					
Total shots	Total traces	Samples/trace	Sampling rate [s]	Ormsby bandpass filter [Hz]	Notch filter [Hz]
60	3600	4000	0.5	20-40-80-160	NA
S-wave dataset information					
Total shots	Total traces	Samples/trace	Sampling rate [s]	Ormsby bandpass filter [Hz]	Notch filter [Hz]
60	3600	4000	0.5	8-16-32-64	7.5, 15, 30

Table 2: GPS locations of geophones along the seismic profile.

Stns.	Latitude	Longitude	Elevation [m]	Stns.	Latitude	Longitude	Elevation [m]
1	37.65550	-122.05260	161.7	31	37.65674	-122.05193	159.5
2	37.65554	-122.05257	161.7	32	37.65678	-122.05191	159.4
3	37.65558	-122.05256	161.6	33	37.65682	-122.05189	159.4
4	37.65562	-122.05253	161.5	34	37.65687	-122.05186	159.3
5	37.65566	-122.05251	161.3	35	37.65691	-122.05184	159.3
6	37.65571	-122.05248	161.1	36	37.65695	-122.05182	159.2
7	37.65575	-122.05246	161.0	37	37.65699	-122.05180	159.3
8	37.65579	-122.05244	160.9	38	37.65703	-122.05178	159.5
9	37.65583	-122.05242	160.7	39	37.65707	-122.05175	159.6
10	37.65587	-122.05239	160.6	40	37.65712	-122.05173	159.7
11	37.65591	-122.05237	160.5	41	37.65716	-122.05171	159.8
12	37.65595	-122.05235	160.4	42	37.65720	-122.05169	160.0
13	37.65599	-122.05233	160.3	43	37.65724	-122.05166	160.3
14	37.65604	-122.05231	160.2	44	37.65728	-122.05164	160.5
15	37.65608	-122.05228	160.1	45	37.65732	-122.05162	160.7
16	37.65612	-122.05226	160.1	46	37.65736	-122.05160	160.9
17	37.65616	-122.05224	160.0	47	37.65741	-122.05158	161.0
18	37.65620	-122.05221	159.9	48	37.65745	-122.05156	161.1
19	37.65624	-122.05219	159.9	49	37.65749	-122.05153	161.3
20	37.65629	-122.05217	159.9	50	37.65753	-122.05151	161.4
21	37.65633	-122.05215	159.8	51	37.65757	-122.05149	161.6
22	37.65637	-122.05213	159.7	52	37.65761	-122.05147	161.8
23	37.65641	-122.05211	159.7	53	37.65765	-122.05144	161.9
24	37.65645	-122.05208	159.7	54	37.65770	-122.05142	162.0
25	37.65649	-122.05206	159.7	55	37.65774	-122.05140	162.1
26	37.65654	-122.05204	159.6	56	37.65778	-122.05138	162.3
27	37.65658	-122.05202	159.6	57	37.65782	-122.05136	162.6
28	37.65662	-122.05199	159.5	58	37.65786	-122.05134	162.8
29	37.65666	-122.05197	159.5	59	37.65790	-122.05131	163.0
30	37.65670	-122.05195	159.5	60	37.65794	-122.05129	163.2

Table 3: Groundwater elevation data from closely spaced monitoring well both east and west of the Hayward Fault, near Quarry Lakes, Fremont, CA. Data from Alameda County Water District Final 2017 Groundwater Monitoring Report.

	Well Number	Sample Date	Water Elevation (ft)	Water Elevation (m)	Sample Date	Water Elevation (ft)	Water Elevation (m)
East of HF	4S/1W-21R002	--	--	--	--	--	--
	4S/1W-27D008	3/28/2017	47.97	14.62	9/26/2017	40.35	12.31
West of HF	4S/1W-28D002	--	--	--	--	--	--
	4S/1W-29A006	3/28/2017	18.56	5.66	9/26/2017	14.28	4.36

	3/28/17	9/26/2017
Difference in groundwater elevation (ft, m) east of the HF relative to the west side.	(ft)	(ft)
	29.41	26.07
	(m)	(m)
	8.96	7.95